

Effect of phase change on jet atomization: a direct numerical simulation study

Xinxin Gao¹, Jianye Chen^{1,†}, Yanan Qiu², Yue Ding¹ and Junlong Xie¹

¹School of Energy and Power Engineering, Huazhong University of Science and Technology, Wuhan 430074, PR China

²State Key Laboratory of Technologies in Space Cryogenic Propellants, Beijing 100028, PR China

(Received 7 May 2021; revised 7 November 2021; accepted 23 December 2021)

Atomization is often accompanied by phase change, which could significantly affect performance parameters such as the cooling efficiency and combustion efficiency of atomization. Nevertheless, the effect of phase change on jet atomization is rarely numerically studied due to the complexity of the coupling of the aerodynamics and the thermodynamics as well as the modelling difficulty caused by the cross-scale flow. In this study, comprehensive direct numerical simulations were carried out to evaluate the effects of phase change on the primary breakup and secondary atomization. Two methods dealing with phase-interface movement and mass transfer across the interface are built to meet the requirements of different modelling scales and Weber numbers. Simulation results indicate that phase change affects the flow behaviours and volume distribution of broken droplets in the primary breakup. In the secondary atomization, phase change leads to significantly different deforming morphologies of droplets with low Weber number and a more thorough breakup of droplets with high Weber number.

Key words: aerosols/atomization, computational methods, gas/liquid flow

1. Introduction

Atomization is a common phenomenon in applications such as cryogenic wind tunnels, aerospace engines and spray cooling. The quality of atomization often determines some important performance parameters. For example, the cooling efficiency in spray cooling is directly affected by the droplet distribution and atomization cone angle (Liu *et al.* 2017). Therefore, it is essential to clarify the atomization mechanism and related physics for scientific and practical applications. Literature survey shows that it remains challenging to explain the jet atomization process affected by the aerodynamic effect. Moreover, the coupling with thermodynamic effects such as evaporation and flash boiling makes this process more complex. In short, the research on atomization mechanisms and

† Email address for correspondence: jianye_chen@hust.edu.cn

the prediction of atomization characteristics are the hotspots and difficulties of past decades.

The atomization process is usually divided into primary breakup and secondary atomization. In primary breakup, the liquid jet is broken into ligaments and drops under the effect of aerodynamics and turbulence. Subsequently, these ligaments and droplets further break, collide or coalesce to form smaller droplets, known as secondary atomization. Atomization has been studied for more than a century, and numerous theoretical (Lin & Lian 1990; Yang 1992; Gordillo, Pérez-Saborid & Gañán-Calvo 2001), experimental (Linne *et al.* 2006; Wang *et al.* 2016; Heindel 2018) and numerical simulation (Lebas *et al.* 2006; Hoyas *et al.* 2013; Anez *et al.* 2019) studies have been carried out. Compared with numerical investigations, theoretical research is limited to predicting a certain part of atomization, and in experimental research it is currently difficult to observe the breakup details of jet, ligaments and drops. Early numerical studies mainly employed the Lagrangian–Eulerian method and focused on atomization characteristics. The empirical atomization models such as the blob model (Reitz 1987) in the primary breakup, and the Taylor analogy breakup (TAB; O’Rourke & Amsden 1987), droplet deformation and breakup (DDB; Ibrahim, Yang & Przekwas 1993) and Rayleigh Taylor (RT; Patterson & Reitz 1998) models in secondary atomization were consequently proposed. However, some fundamental issues such as the atomization mechanism and the evolution of gas–liquid interface have not been concluded.

1.1. Direct numerical simulation of jet atomization

With the rapid development of computer technology in recent years, it has become possible to establish a high-precision simulation of atomization using direct numerical simulation (DNS) and interface capture methods (volume of fluid (VOF), level set). However, DNS modelling of the entire spray process, including the primary breakup and secondary atomization, is still beyond current computational capacity. Therefore, most studies only focus on the primary breakup near the nozzle or the secondary atomization downstream.

For the primary breakup, DNS research has significantly advanced our understanding of the breakup mechanism. Herrmann (2011) simulated the primary breakup of a liquid injected into a static high-density gas environment using the refined level set grid method. The results show that turbulence is one of the driving factors for liquid breakup near the nozzle, and the statistical distribution of the droplets in the simulation is closely related to the resolution of the grid. Shinjo & Umemura (2010, 2011*a,b*) studied several physical phenomena such as the formation of ligaments, development of surface unstable waves and the production of liquid droplets in a high-speed jet. Jarrahbashi & Sirignano (2014) studied the vortex dynamics in the primary breakup of a cylindrical jet and suggested that the circumferential instability of the jet was related to the vortex. Zandian, Sirignano & Hussain (2017, 2018, 2019) further analysed the vortex dynamics of the primary breakup process of a plane jet and a cylindrical jet. Based on the liquid Reynolds number (Re_l) and gaseous Weber number (We_g), three main atomization mechanisms with different characteristic lengths and time scales were defined. The effects of inertial force, vortex, pressure, viscosity and surface tension on the three-dimensional (3-D) instability of the axisymmetric Kelvin–Helmholtz (K–H) structure were also evaluated. Agarwal & Trujillo (2018) studied the breakup of a jet surface and core using the VOF method and compared it with the Orr–Sommerfeld linear stability theory. They showed that the prediction of the most unstable wave near the nozzle in simulation is consistent with the theory, but the linear theory only acts on the jet surface instead of the jet core. Salvador *et al.*

(2018) numerically analysed the effect of different boundary conditions on atomization by imposing synthetic turbulence boundary conditions.

To reduce the grid number and improve the computational efficiency, an adaptive mesh algorithm (AMR) based on octree grids (Popinet 2009) was applied in the atomization simulation. Fuster *et al.* (2009) used AMR to simulate primary breakup under different Reynolds numbers. The results show that the numerical result is consistent with the linear theory in the modelling of multiscale complex interface deformation. Yang & Turan (2017) studied the effect of forced disturbance on the atomization of high-speed and low-speed jets using the VOF method based on AMR grids. The results indicate that the jet has a more obvious response to low-frequency disturbance, which also has a greater effect on the atomization characteristics.

For the secondary atomization, DNS studies mainly focused on the investigation of droplet deformation and breakup. Jalaal & Mehravaran (2012) classified the droplet-breakup mechanisms into deformation, bag formation and bag breakup by carrying out DNS modelling of droplets falling in a static gas environment. Khare *et al.* (2013) evaluated the effects of physical properties on different breakup forms of a Newtonian liquid droplet under high pressure. Accordingly, a generalized state diagram using the simulation data was summarized to predict the breakup mode of Ohnesorge number (Oh) < 0.1 . Shao, Luo & Fan (2017) performed a detailed numerical simulation of the unsteady drag coefficient of deformable droplets using the mass conservation level-set method. It was found that the unsteady drag coefficient is always greater than the steady standard drag coefficient. And droplet deformation and acceleration variation have the largest impact on the unsteady drag coefficient, followed by the Weber number. Jain *et al.* (2019) numerically studied the effect of the density ratio and Reynolds number on the dynamics of droplet deformation under medium We number (20–120). A phase diagram of density ratio–Weber number was proposed, reflecting the variation in droplet deformation with different parameters.

1.2. Phase-change numerical methods in DNS

The jet breakup and atomization are usually accompanied by strong evaporation. Most of the abovementioned DNS studies on the atomization mechanism only focused on the analysis of jet flow with mechanical effects and ignore the thermodynamic processes. To the best of our knowledge, the mechanism of primary breakup and secondary atomization under phase-change conditions has rarely been reported. It is often believed that the time scale of the jet breakup is much smaller than that of phase change so that phase change has a negligible effect. However, the numerical results reported by Huang & Zhao (2019) show that the breakup and atomization characteristics in a high-temperature environment are significantly different from those in a low-temperature environment. Unfortunately, only the macroscopic characteristics such as temperature and vapour mass fraction distribution have been analysed. The microscopic breakup mechanism remains to be elucidated.

The interface movement accompanied by heat and mass transfer across the interface is one of the biggest challenges in the DNS modelling of atomization with phase change. The coupling of empirical formulas and governing equations is simple and widely used (Jeon, Kim & Park 2011; Pan *et al.* 2012). However, these methods cannot accurately simulate the heat and mass flux across the gas–liquid interface due to the limitation of empirical parameters. Therefore, more accurate numerical methods based on DNS have been proposed to determine the heat and mass transfer as well as the jump of various physical quantities across the interface. The methods can be classified into two types as follows.

The first one discretely deals with the jump of the physical quantities across the interface using the ghost-fluid method, and the capture of the interface with the level-set method. Gibou *et al.* (2007) simulated the evaporation of 2-D droplets based on the level-set method. The Dirichlet boundary condition was applied at the interface to solve the energy equation assuming the interface temperature equal to the saturation temperature. Tanguy, Ménard & Berlemont (2007) conducted a numerical study on the evaporation of both stationary and moving droplets in the air. The evaporation rate was calculated according to the mass fraction gradient at the interface. Rueda Villegas *et al.* (2016) proposed a numerical method that considers both interface boiling and evaporation. The energy and mass fraction equations are coupled through thermodynamic analysis, and the non-uniform Dirichlet and Robin boundary conditions are used at the interface.

The second type of method continuously models the interface based on the VOF interface convection framework. Each physical quantity continuously varies near the interface in this method. Hardt & Wondra (2008) reported a vaporization algorithm and applied a mass source term at the interface to describe the phase-change mass transfer. Taking into account the pressure fluctuations that may be caused by the point source term in the VOF sharpening interface method, they used the non-homogeneous Helmholtz equation to alleviate this problem, which can smooth the mass flux around the interface. Georgoulas, Andredaki & Marengo (2017) further extended the Hardt & Wondra's (2008) method, separating the heat and mass transfer from interface localization by deleting the mass flux source term in the grid containing the interface. The quantitative effects of basic control parameters on the detachment characteristics of isolated bubbles in pool boiling were investigated. Similarly, Wang & Yang (2019) artificially set a sink layer in the liquid phase and a source term layer in the gas phase close to the interface to evaluate the source terms in the mass, energy and composition equations. This method has the advantages of high accuracy and easy implementation compared with the traditional method of directly processing phase changes at the interface.

In addition, new methods based on other interface-capturing methods or interface jump processing have been proposed. Sato & Ničeno (2013) reported a new phase-change numerical methods based on the mass conservation interface tracking method. The speed jump across the interface can be accurately captured owing to the sharp distribution of mass transfer. Malan (2018) solved the liquid velocity at the interface by dividing a subdomain at the interface. The technique effectively solves the conservation problem of the geometric VOF convection method owing to the discontinuity of the velocity at the interface. Lee, Riaz & Aute (2017) proposed a new hybrid method that combines the smooth processing of mass flux with the sharp processing of speed jumps, surface tension, momentum recoil and temperature gradient to solve the pressure fluctuations at the interface to a certain extent.

1.3. Problems and objectives

The following problems need to be settled for establishing a DNS study of atomization with phase change: (i) the great scale span of the primary breakup and secondary atomization makes the complete simulation of jet atomization an almost impossible task with the current computational performance; (ii) a sharp normal velocity jump across the interface (also called Stefan flow) due to the gas–liquid phase change significantly affects the temperature field. In reverse, the precision of phase-change method is directly determined by the accurate calculation of the temperature gradient near the interface; (iii) due to the complex deformation of the interface and cross-scale conditions in breakup,

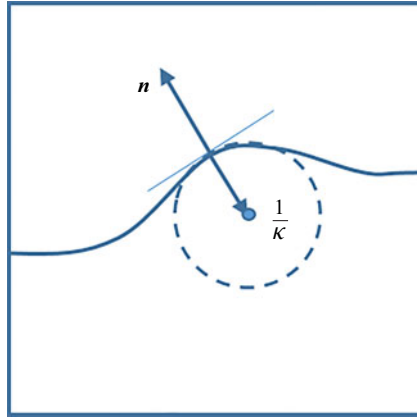


Figure 1. Schematic diagram of interface normal vector \mathbf{n} and interface curvature κ . The dotted circle in the figure is the curvature circle, and the radius of the circle is the curvature radius $r = 1/\kappa$.

the small droplets generated by atomization occupy only a few grids, causing additional challenges to the phase-change modelling process.

To overcome the abovementioned difficulties, this study separately performs the primary breakup and secondary atomization processes. The primary breakup and the secondary atomization with high We number are simulated using an interface shift method (ISM) is to decouple the mass transfer and velocity fields. The effect of the Stefan flow is ignored considering that the inertial effect is much greater than the phase-change effect. For low We secondary atomization, we build a source term diffusion method (STDM) to couple mass transfer separation from interface localized and sharpening interface temperature techniques. STDM relieves the pressure fluctuations while ensuring the calculation accuracy of the mass flux rate. Moreover, it can accurately simulate the heat and mass transfer and the speed jump across the interface. The simulations are achieved in a well-developed geometric VOF based software ‘Basilisk’, which employs an adaptive mesh technology to reduce the number of grids. The accuracy of the two phase-change methods was verified through several examples, and then investigations of primary breakup and secondary atomization are carried out.

2. Numerical methods

2.1. Governing equations

The two-phase 3-D incompressible Navier–Stokes (N-S) equation can be expressed as follows:

$$\rho(\partial_t \mathbf{u} + \mathbf{u} \cdot \nabla \mathbf{u}) = -\nabla p + \nabla \cdot (2\mu \mathbf{D}) + \sigma \kappa \delta_s \mathbf{n}, \quad (2.1)$$

where \mathbf{u} is the velocity vector, ρ is the fluid density, p is the pressure, μ is the fluid viscosity and \mathbf{D} is the deformation rate tensor defined by

$$\mathbf{D} = \frac{1}{2}[(\nabla \mathbf{u}) + (\nabla \mathbf{u})^T]. \quad (2.2)$$

The last term in (2.1) denotes the surface tension term, where σ is the surface tension coefficient, κ is the surface curvature and δ_s is the Dirac-delta function, \mathbf{n} is the normal vector at the interface as shown in figure 1, so that the surface tension only acts on the phase interface.

The continuity equation can be expressed as follows:

$$\nabla \cdot \mathbf{u} = 0. \tag{2.3}$$

Using the VOF method to capture the gas–liquid interface, the volume fraction is convective with the velocity field. The transport equation yields

$$\partial_t f + \nabla \cdot (f\mathbf{u}) = 0, \tag{2.4}$$

where f denotes the volume fraction of the liquid phase. The physical properties in the flow field can be calculated from the local volume fraction

$$\left. \begin{aligned} \rho(f) &\equiv f\rho_l + (1-f)\rho_v \\ \mu(f) &\equiv f\mu_l + (1-f)\mu_v \end{aligned} \right\}, \tag{2.5}$$

where the subscripts l and v represent liquid and gas, respectively.

The temperature distribution has a decisive effect on the phase-change process. By ignoring the viscous dissipation, the energy equation describing the temperature field variation can be written as follows:

$$\rho c_p \left(\frac{\partial T}{\partial t} + \mathbf{u} \cdot \nabla T \right) = \nabla \cdot (\lambda \nabla T), \tag{2.6}$$

where T is the temperature field, c_p is the heat capacity of the fluid and λ is the thermal conductivity.

When phase change occurs, the liquid portion passes across the interface with a certain mass flow rate and expands to form vapour. The relationship between local mass flow rate per unit area \dot{m} , interface velocity u_Γ and the velocity of gas and liquid phase can be obtained according to the conservation of mass

$$\rho_l(\mathbf{u}_\Gamma - \mathbf{u}_l) \cdot \mathbf{n} = \rho_v(\mathbf{u}_\Gamma - \mathbf{u}_v) \cdot \mathbf{n} = \dot{m}. \tag{2.7}$$

Therefore, the normal velocity jump conditions on both sides of the interface can be obtained as follows:

$$\mathbf{u}_v - \mathbf{u}_l = \left(\frac{1}{\rho_v} - \frac{1}{\rho_l} \right) \dot{m} \mathbf{n}, \tag{2.8}$$

where \dot{m} can be determined from the heat flow on both sides of the interface

$$\dot{m} = \frac{(\mathbf{q}_l - \mathbf{q}_v) \cdot \mathbf{n}}{h_{fg}} = \frac{((\lambda \nabla T)_l - (\lambda \nabla T)_v) \cdot \mathbf{n}}{h_{fg}}, \tag{2.9}$$

where h_{fg} represents the latent heat.

In the mixing cell containing the interface, the continuity equation is corrected according to the speed jump condition due to the phase change

$$\nabla \cdot \mathbf{u} = \left(\frac{1}{\rho_v} - \frac{1}{\rho_l} \right) \ddot{m}, \tag{2.10}$$

where \ddot{m} is the source term of mass transfer per unit volume, which can be obtained by transforming the local mass flow rate

$$\ddot{m} = \dot{m} \delta_\Gamma, \tag{2.11}$$

where δ_Γ is the interfacial surface area density which can be defined as follows:

$$\delta_\Gamma = \frac{S_\Gamma}{V_{cell}}, \tag{2.12}$$

where S_Γ is the area of phase interface in the mixing cells, and $V = 5$ is the volume of the mixing cell.

2.2. Numerical methods

1) Projection method for N-S equation and geometric VOF convection method

The incompressible N-S equation is solved using the projection method, and the geometric VOF convection method is used to capture the phase interface. The detailed numerical method can be found in Popinet (2003, 2009). The second-order staggered discretization is used in the unsteady term, and the solution is divided into two steps. Firstly, a temporary velocity is calculated by ignoring the effect of pressure

$$\rho^{n+1/2} \left[\frac{\mathbf{u}^* - \mathbf{u}^n}{\Delta t} + \mathbf{u}^{n+1/2} \cdot \nabla \mathbf{u}^{n+1/2} \right] = \nabla \cdot [\mu^{n+1/2} (\mathbf{D}^n + \mathbf{D}^*)] + (\sigma \kappa \delta_s \mathbf{n})^{n+1/2}. \tag{2.13}$$

Subsequently, the speed is corrected by considering the effect of pressure as follows:

$$\mathbf{u}^{n+1} = \mathbf{u}^* - \frac{\Delta t}{\rho^{n+1/2}} \nabla p^{n+1/2}. \tag{2.14}$$

The velocity field satisfies the continuity equation as follows:

$$\nabla \cdot \mathbf{u}^{n+1} = 0. \tag{2.15}$$

Coupling (2.14) with (2.15), the Poisson equation for solving the pressure field can be obtained as follows:

$$\nabla \cdot \left[\frac{\Delta t}{\rho^{n+1/2}} \nabla p^{n+1/2} \right] = \nabla \cdot \mathbf{u}^*. \tag{2.16}$$

The geometry VOF advection method is used to describe the interface. The Eulerian implicit–explicit format is used in time discretization. The piecewise linear interface construction (Scardovelli & Zaleski 1999) method is applied and the interface normal is computed by the mixed-Youngs-Centred method (Aulisa *et al.* 2007). The location of the interface in the cell is calculated based on the method of Scardovelli and Zaleski (Scardovelli & Zaleski 2000). The multi-dimensional VOF advection scheme uses dimension splitting (Weymouth & Yue 2010) i.e. advects the field along each dimension successively using a 1-D scheme. An interface reconstruction is performed to avoid numerical diffusion after completing the update in each direction. The discrete format can be expressed as follows:

$$\frac{f^{n+1/2} - f^{n-1/2}}{\Delta t} + \nabla \cdot (f^n \mathbf{u}^n) = 0. \tag{2.17}$$

2) Phase-change numerical methods

A. Interface shift method

The ISM considers the volume change of two phases by ignoring the Stefan flow during the phase change. The basic idea is to calculate the shift velocity of the interface \mathbf{u}_I according to the mass flow rate. By superimposing \mathbf{u}_I with the original velocity field, it solves the VOF convection equation, and then restores the velocity field. More details about the numerical method are attached in Appendix A.1

$$\mathbf{u}_I = \frac{((\lambda \nabla T)_l - (\lambda \nabla T)_v) \cdot \mathbf{n}}{\rho_l h_{fg}}. \tag{2.18}$$

The ISM directly changes the position of the interface to achieve the phase change, so the mass conservation issue in it needs to be further explored. The detailed description

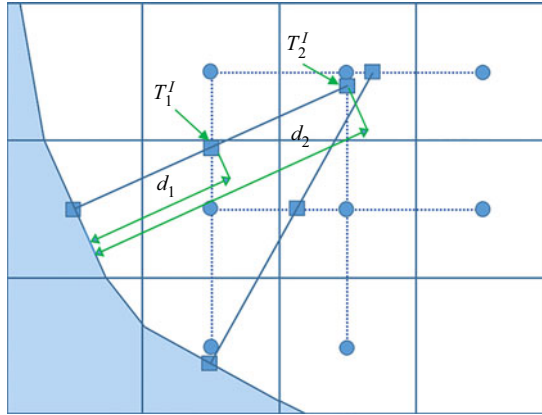


Figure 2. Second-order stencil of interface normal gradient. Here, T_1^I and T_2^I are two interpolation points obtained by quadratic interpolation of three points (circle points) on vertical lines (the angle between the interface normal and the horizontal plane is less than 45°). Otherwise, we use three points on the horizontal line; d_1, d_2 are the distances from the two intersection points to the interface, respectively.

of this method can be found in Magdelaine (2019b), and the source code and verification examples can be browsed in Magdelaine’s sandbox (Magdelaine 2019a).

B. Source term diffusion method

In the secondary atomization, the velocity of the droplets produced by the primary breakup decreases under the action of aerodynamic resistance. Therefore, the phase change has an important influence on the flow field at a low We number, and the relatively smooth deformation interface of the low-velocity droplets reduces the difficulty of modelling. A new phase-change method (STDM) was established to describe the flow jump near the interface. STDM applies Dirichlet boundary conditions to the gas–liquid interface to sharpen the temperature field and improve the accuracy of the heat and mass transfer flux calculations.

First, \dot{m} was also obtained according to (2.9) at the interface. The calculation of heat flow requires the determination of temperature gradients on both sides of the interface. To ensure the accuracy of the gradients, unlike Magdelaine’s (2019b) approximate estimation, we employ a second-order-precision gradient calculation method, which uses data in the pure liquid or gas cells for calculation. The first pair of parallel grid lines are selected that intersect with the line normal to the interface, but the grid lines do not pass through the current cell, as shown in figure 2. The values of the two intersections can be obtained by quadratic interpolation (biquadratic interpolation in three dimensions). Subsequently, the gas or liquid temperature gradient at the interface can be obtained as follows:

$$\frac{\partial T}{\partial n} = \frac{1}{d_2 - d_1} \left(\frac{d_2}{d_1} (T_\Gamma - T_1^I) - \frac{d_1}{d_2} (T_\Gamma - T_2^I) \right), \tag{2.19}$$

where T_Γ is the phase interface temperature with the assumption of the system remaining at the saturation temperature (i.e. $T_\Gamma = T_{sat}$) during the phase change. For a few special cells where T_1^I, T_2^I cannot be obtained in a complex interface flow simulation, this stencil is unavailable. For the degenerate cases (T_1^I, T_2^I cannot be calculated), the gradient is defined using the boundary value and the cell-centre value. For the case such that T_2^I cannot be calculated, a lower-order stencil is employed.

Effect of phase change on jet atomization

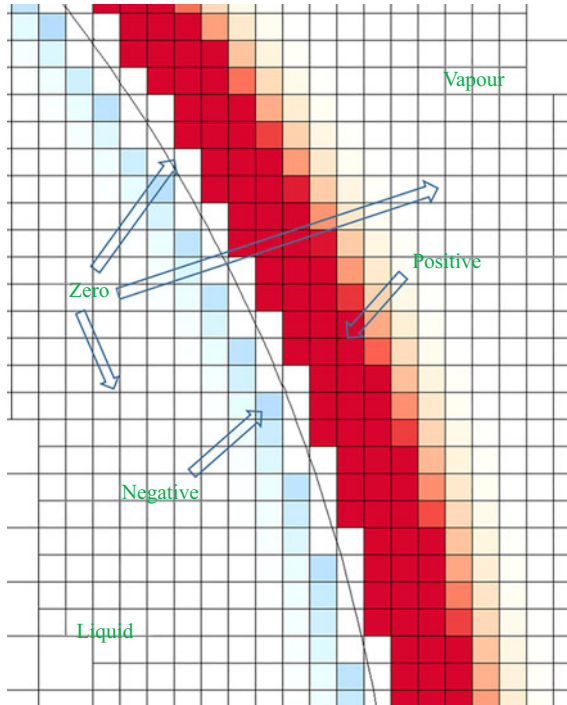


Figure 3. Distribution of source terms in the computational domain. The red area on the gas side has a positive mass transfer source term. The blue one in liquid represents the negative source term. The source term is equal to 0 in cells far away from the interface or including the interface.

Then, the mass source term can be calculated using (2.9) and (2.11). However, the mass source term only acts on the mixing cell, which will cause pressure parasitic fluctuations when solving the pressure Poisson equation. Hardt & Wondra (2008) proposed a method for diffusing the source term, making the source term more evenly distributed in the multilayer grid near the interface to alleviate the instability. In this study, a similar method was used by adding a negative mass source term to the liquid phase close to the interface to simulate the recession of the interface to the liquid side during phase change. At the same time, an equivalent positive mass source term was added to the vapour side to simulate the volume expansion of the liquid. See Appendix A.2 for more details, and finally the mass transfer source was obtained as (2.20). The distribution of source term in the calculation domain is shown in figure 3

$$\dot{m} = N_v H_v (0.5 - f) \dot{m}_1 - N_l H_l (f - 0.5) \dot{m}_1, \quad (2.20)$$

where N_v, N_l is the scale factor for vapour and liquid respectively, H is the Heaviside function. Then, modifying the continuity equation as follows:

$$\nabla \cdot \mathbf{u} = \frac{\dot{m}}{\rho}. \quad (2.21)$$

The corrected pressure Poisson equation can be obtained by coupling (2.21) with (2.14)

$$\nabla \cdot \left[\frac{\Delta t}{\rho^{n+1/2}} \nabla p^{n+1/2} \right] = \nabla \cdot \mathbf{u}^* - \frac{\dot{m}}{\rho}. \quad (2.22)$$

The accurate solution of the temperature field is the key to evaluating the phase-change process. The temperature field depends on the velocity field and the temperature field also reacts onto the velocity field because the mass flow rate is calculated from the temperature gradient. The main challenge in solving this problem is how to keep the interface temperature equal to the saturation temperature. Here, an embed boundary method (Johansen & Colella 1998) was used, which applies the Dirichlet boundary at the gas–liquid interface, and energy equations of gas and liquid phases are solved respectively. The energy equation can be discretized as follows:

$$\frac{T^{n+1/2} - T^{n-1/2}}{\Delta t} + (\mathbf{u} \cdot \nabla T)^{n+1/2} = \nabla \cdot \left(\left(\frac{\lambda}{\rho c_p} \right) \nabla T \right)^{n+1/2}. \quad (2.23)$$

The calculation of the convection term is similar to that of the VOF convection equation. A detailed description can be found in Popinet (2009). The diffusion term is discretized using the finite volume method and the boundary condition is that considered in the discretization format of the grid containing the interface, as in (2.24). The detailed numerical method can be found in Appendix A.3

$$\alpha \nabla \cdot \nabla T = \frac{\alpha}{\Delta x \Delta y f_{i,j}} (F_{i+1/2,j} - F_{i-1/2,j} + F_{i,j+1/2} - F_{i,j-1/2} - F_{i,j}^T), \quad (2.24)$$

where $\alpha = \lambda/\rho c_p$ is the thermal diffusivity; Δx and Δy are the length and width of the grid, respectively. The subscripts i and j represent the grid label.

The calculation steps of each time step of STDM are summarized as follows:

- (i) Using (2.19), calculate the gas–liquid normal gradient at the interface and then determine the phase-change mass flow rate from (2.9).
- (ii) Diffuse the mass flow source term to obtain the final volume source term field \dot{m} . Solve the VOF convection equation and energy equation convection term, and use \dot{m} to modify the continuity equation.
- (iii) Using the approximate projection method, update the velocity and pressure field at the next step.
- (iv) Apply the Dirichlet boundary condition at the interface by the embedded boundary method to solve the diffusion term of the energy equation.

3. Method validation

The validation cases use different mesh resolutions, and the related information is given in Appendix B.1. Although Basilisk has been extensively verified as a two-phase flow solver, a second atomization experiment (Flock *et al.* 2012) is used to conduct the validation in the present work. The results are in good agreement with experiment, and validation can be found in Appendix B.2.

3.1. Stefan problem

The Stefan problem was first used by Welch & Wilson (2000) to validate their phase-change numerical methods successfully, and it has since been widely used in the validation of incompressible phase-change simulations. The physical model of Stefan problem is shown in figure 4. The liquid temperature at the initial moment is set as the saturation temperature, and the wall is superheated with a certain degree. A thin vapour layer exists between the liquid and wall, whose thickness increases with phase

Effect of phase change on jet atomization

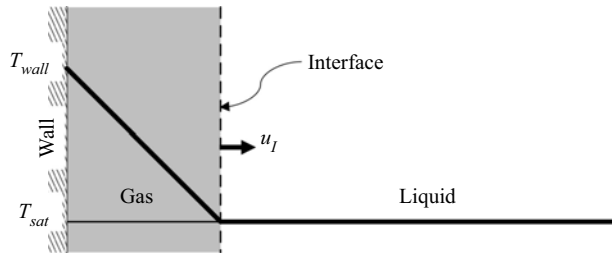


Figure 4. Stefan problem test case. There is a vapour layer between the superheated wall and the liquid, in which the temperature is linearly distributed. The vapour layer continues to grow under the action of phase change.

	ρ kg m ⁻³	c_p J (kg K) ⁻¹	μ Pa s	λ W (m K) ⁻¹	σ N m ⁻¹
Liquid	958.4	4216	2.82×10^{-4}	0.68	0.059
Vapour	0.597	2030	1.23×10^{-5}	0.025	

Table 1. Physical properties of water ($P = 101.3$ kPa, $T = 373$ K).

change driven by the temperature gradient. Ignoring the effect of gravity, the face-to-face boundary of the hot wall is set as a free flow condition. This problem has an analytical solution that can be found in [Appendix B.3](#).

The calculation domain size is set as 10 mm \times 10 mm, and the wall superheat is 10 K. The main physical parameters are shown in [table 1](#). In order to avoid the influence of the initial transient behaviour and describe the temperature field accurately, the simulation starts at 0.2824 s with an existing vapour-layer thickness equal to 0.3225 mm according to the analysis solution.

[Figure 5](#) shows a comparison between the numerical vapour-layer thicknesses by the two methods with different grid resolutions and the analytical results. It indicates that the numerical simulation results are always consistent with the analytical solution with all three different resolutions. [Figure 6](#) shows the temperature distribution with different resolutions. The temperature distribution slightly deviates from the analytical solution with a sparse grid (Level = 6). With a fine grid (Level = 8), the numerical modelling performs completely consistent with the analytical solution.

3.2. Bubble growth under no gravity

Simulation of the growth of a single bubble under no gravity conditions was also conducted to verify the accuracy of the numerical methods. The temperature of a spherical bubble is the saturation temperature at the initial moment. The liquid temperature is superheated with a certain degree of superheat, providing the required latent heat for the phase change. Scriven (1959) theoretically derived an analytical solution for the bubble growth, which was then widely used in boiling-related numerical simulation verifications. The analytical solution can be found in [Appendix B.4](#).

By ignoring the effect of gravity, the bubble growth in superheated water at 101 kPa was simulated, and the physical properties are consistent with those in [§ 3.1](#), as shown in [table 1](#). The liquid superheat is 2 K, and the initial radius of bubble is 20 μ m, corresponding to the moment $t = 0.023$ ms in the analytical solution. The temperature

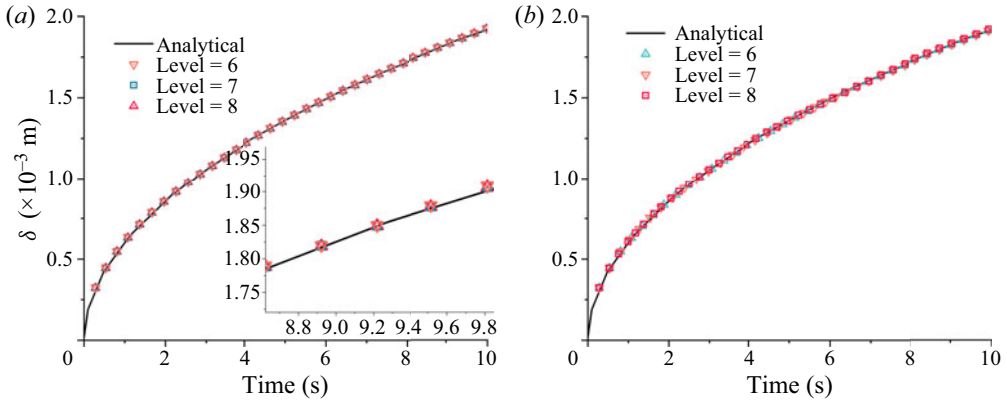


Figure 5. Variation in interface position in numerical and analytical calculations. Level denotes grid refinement level. The black solid line is the analytical solution, and the coloured dots are the simulation results at different resolutions. (a) ISM and (b) STDM.

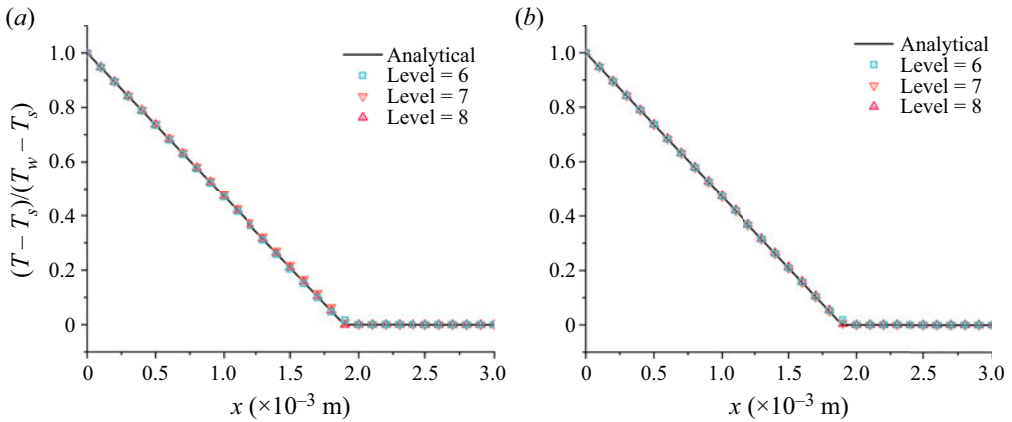


Figure 6. Temperature distribution at $t = 9.75$ s with different grid resolutions. Here, the Y-axis represents the dimensionless temperature $(T - T_s)/(T_w - T_s)$. (a) ISM and (b) STDM.

distribution at this moment was calculated from the analytical solution, providing the initial temperature field for the numerical simulation. The results show that the thickness of the temperature boundary layer is approximately $5.2 \mu\text{m}$. The calculation domain size is $400 \mu\text{m}$, and three different grid sizes of Δ equal to $1.56 \mu\text{m}$, $0.78 \mu\text{m}$ and $0.39 \mu\text{m}$ were used in the simulations. The grids were adaptively refined according to the temperature field and volume fraction field to reduce the computational cost.

Figure 7 shows a comparison between the simulated bubble radius variations and the analytical solution. The simulated results of ISM significantly deviate from the analytical results, while the results with STDM gradually converge to the analytical solution as the grid level increases. It is confirmed that the STDM has a significant advantage in the bubble growth problem compared with the ISM. Figure 8 shows the temperature distribution of bubble growth simulated by ISM and STDM at $t = 60 \mu\text{s}$. The temperature boundary layer calculated using the ISM is very thin, while it is slightly thicker when using the STDM. The bubble rapidly grows with ISM owing to the large temperature gradient at the interface according to (2.9).

Effect of phase change on jet atomization

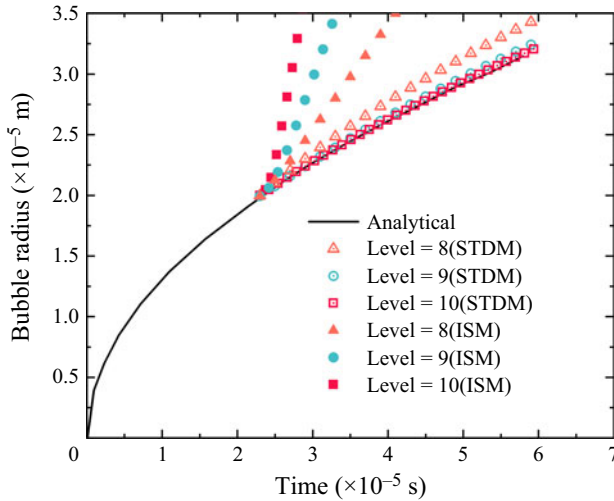


Figure 7. Comparison of bubble radius variation obtained by simulation and analytical solution. The black solid line is the analytical solution, the coloured solid points are the simulation results obtained by using ISM at different resolutions and the hollow points are using STD.

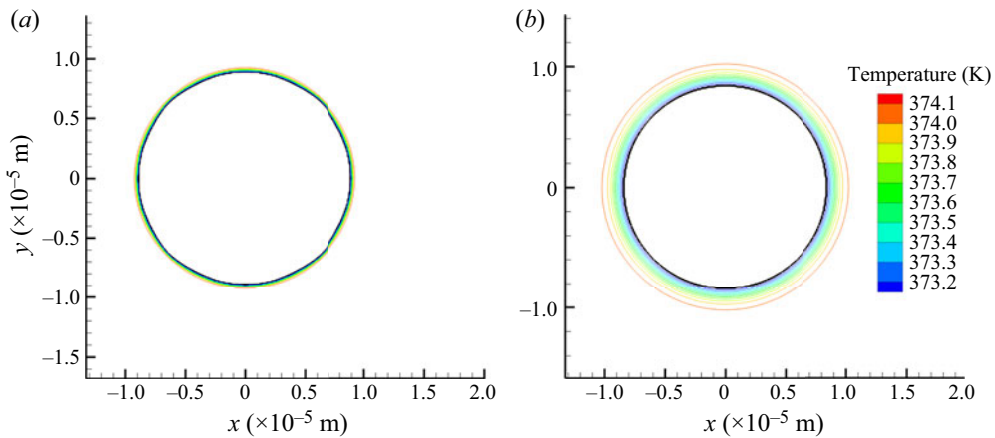


Figure 8. Temperature contour near the bubble at $t = 60 \mu\text{s}$. The black curve refers to the gas–liquid interface, and the coloured ones refer to the temperature contours. (a) ISM and (b) STD.

To gain more insight into the difference between these two methods, the distributions of pressure and velocity vector by the two methods are compared in figure 9. Figure 9(a) reveals that an annular velocity appears near the interface in the simulation with ISM. Considering that ISM ignores the effect of phase change on the velocity field, the annular flow here is artificially caused by the surface tension model. As shown in figure 9(b), an obvious speed jump across the gas–liquid interface occurs, which is also an artificial flow inside the bubble near the interface by STD. The phase-change mass source term distribution shown in figure 10 indicates that the spatial distribution of mass source terms is not uniform due to the limitations of discrete processing of numerical calculations. A relatively large artificial velocity occurs inside the bubble where the mass source term is large. Therefore, it is preliminarily believed that the artificial flow in the simulation with

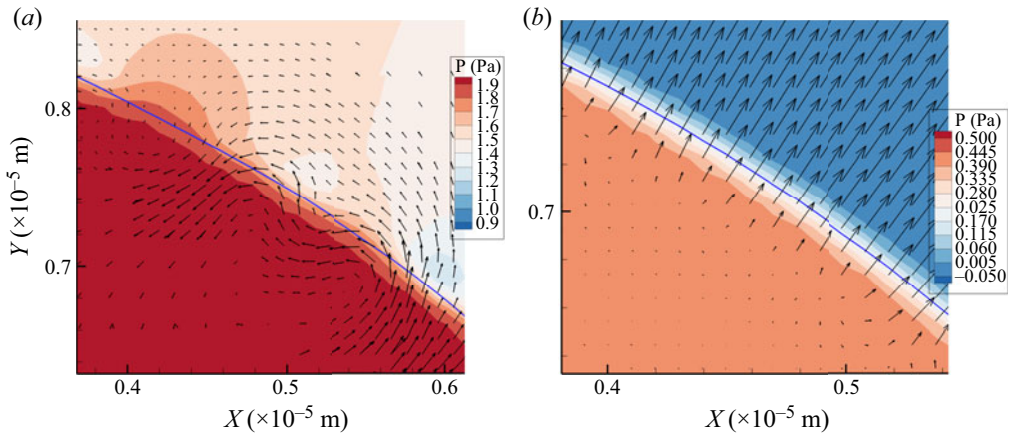


Figure 9. Pressure distribution and velocity vector near the gas-liquid interface at $t = 60 \mu\text{s}$. The solid blue line is the gas-liquid interface, the black arrow is the velocity vector, the left side of the interface is the vapour phase and the right side is the liquid phase. (a) ISM and (b) STDM.

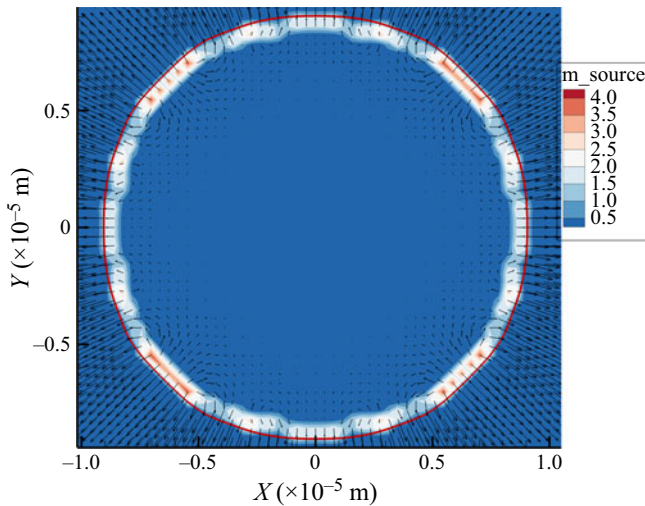


Figure 10. Distribution of phase-change mass source term and velocity vector with STDM at $t = 60 \mu\text{s}$. The red solid line is the gas-liquid interface, and the black arrows are the velocity vectors.

STDM is caused by the uneven distribution of the source term. This phenomenon can be alleviated by refining the grids around the interface. The artificial flow is so small as shown in figures 9(b) and 10 compared with the original velocity field that its impact on the heat and mass transfer simulation can be ignored. Moreover, the mass transfer source terms in the STDM are distributed on both sides of gas and liquid, therefore the gas-liquid pressure shown in figure 9(b) has a smooth transition across the interface. In contrast, the overestimation of mass transfer rate with ISM leads to a sharp increase in the pressure in the bubble. Consequently, the pressure inside the bubble shown in figure 9(a) is significantly higher than that shown in figure 9(b).

Effect of phase change on jet atomization

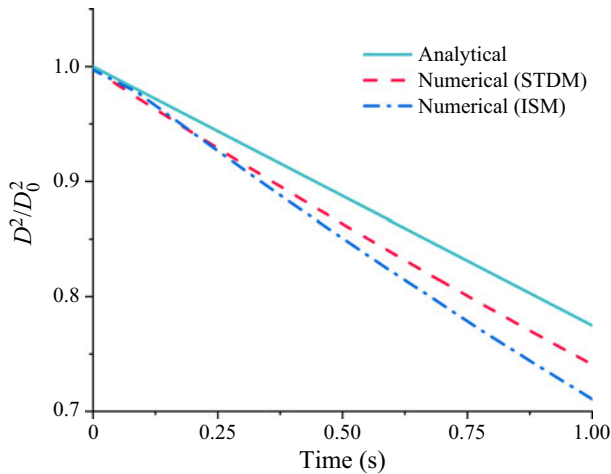


Figure 11. Comparison of simulated result and analytical solution of the D^2 law. At $t = 1$ s, the mass transfer rate (the slope of the curve) obtained by ISM simulation has an error of 13.7% compared with the analytical solution, while for STDM it is 1.8%.

3.3. Phase change of a single drop in a quiescent gas environment

As part of our validation, we examine the vaporization of a single drop in a quiescent gas environment and validate the present methods against the classical ‘ D^2 law’ (Turns 1996). According to Gibou *et al.* (2007) and Chai *et al.* (2018), the properties are determined. The details and the analytical solution are elucidated in Appendix B.5. The initial diameter of the droplet is $d_0 = 0.04$ m; the calculation domain size is $L^2 = 2d_0 \times 2d_0$; and the interface boundary is subject to the Dirichlet boundary condition $T_{bc} = 10$ K.

The phase change was added after the temperature field diffused to a steady state during the simulation. Figure 11 shows a comparison between the drop diameter variation obtained by the two numerical methods and that by the analytical solution. The results indicate that both methods overestimate the phase-change rate at the initial moment, and the drop diameter curves drop faster than the analytical curve. This is attributed to the different assumptions regarding the initial temperature distribution. The temperature distribution is assumed linear in the analytical solution, while it is logarithmic in the simulation, as shown in figure 12 ($t = 0$).

As the phase change proceeds, the simulation results of the STDM gradually show a linear downward trend with the same slope as the analytical solution curve. This is because the Stefan flow is captured at the gas–liquid interface during the phase-change process in the simulation of the STDM, and the temperature distribution gradually evolves into a linear distribution under the effect of convection, as shown by the green curve in figure 12(a). Although the ISM curve has similar downward trends to the STDM curve, the deviation from the analytical solution is greater. In contrast, a large temperature gradient as the green curve in figure 12(b) still exists at the phase interface due to ignoring the Stefan flow in the ISM. As a result, STDM performs better than ISM in the modelling of the phase change of a single drop in a quiescent gas environment.

After verifying the abovementioned multiple examples, the accuracy and robustness of STDM in the calculation of the heat and mass transfer rate and the speed jump across the interface can be confirmed. At the same time, in the comparison of the two methods, STDM behaves better than ISM with smaller errors in the simulation of bubble growth and

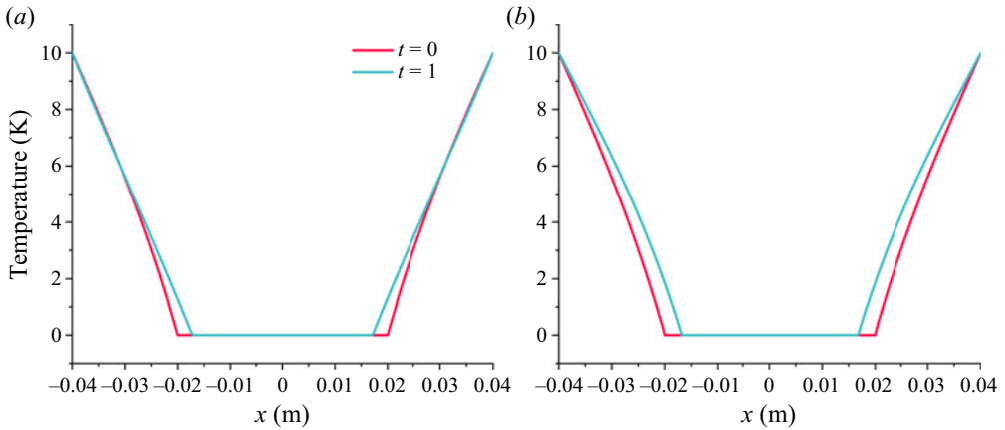


Figure 12. Temperature distribution at different moments. (a) The numerical result with STDM at $t = 0, 1$ s. (b) The numerical result with ISM.

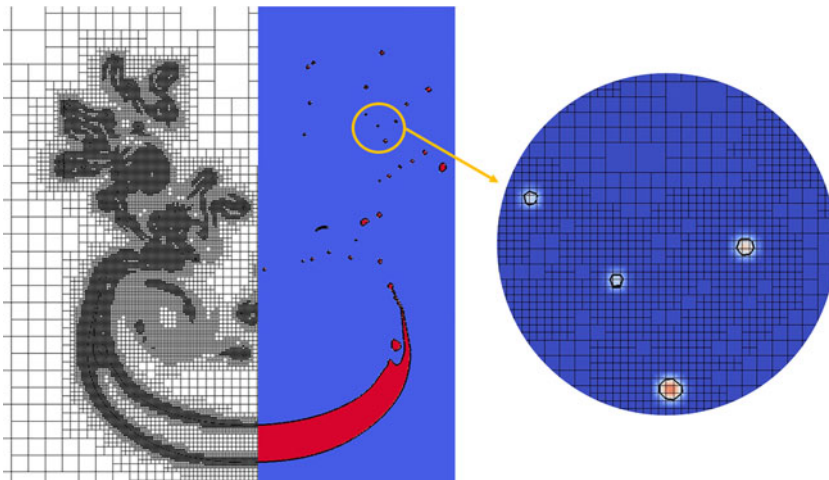


Figure 13. Phase distribution and grids in simulation. The droplet is severely deformed and broken during the atomization, and the AMR technology refines the grid near the interface. The local zoom shows the mesh of the small droplets produced by the fragmentation.

the droplet surface phase change, which is attributed to the consideration of Stefan flow. This error decreases with the growing thermal diffusion coefficient. The prediction of the interface evolution in the droplet vaporization is better than that in the bubble growth. In addition, the atomized droplets generated by the primary breakup or high We number secondary atomization occupy only a few cells, as shown in figure 13, while the STDM requires several layers of grids to place the source term when processing the phase change (as shown in figure 3). Therefore, it is difficult to apply this method in the case of violent atomization, and, at the same time, the error of ISM in droplet surface phase change is within the acceptable range. Considering the above reasons, the ISM was used in this study for the simulation of primary breakup and secondary atomization at middle and high We numbers, while the STDM is used in the deformation of a low We number droplet.

	ρ kg m ⁻³	c_p J (kg K) ⁻¹	μ Pa s	λ W (m k) ⁻¹	σ N m ⁻¹
LN ₂	712	2230	0.000085	0.11	0.0049
GN ₂	24.273	1345	0.0000073	0.01	

Table 2. Physical properties in the calculation ($p = 5.88 \times 10^5$ Pa).

4. Phase change in the primary breakup

4.1. Numerical results of primary breakup

In the DNS modelling of the primary breakup, the jet flow characteristics in a gas environment after leaving the nozzle are investigated without considering the flow behaviour inside the nozzle. In addition, the effect of gravity is ignored. The calculation domain is a cube with a side length of 5 mm, and the spray nozzle is located at the centre of left side of the domain with a diameter (d_0) equal to 0.25 mm. The velocity inlet boundary condition $U_l = 60$ m s⁻¹ is applied. To mimic the disturbance introduced by the flow inside the nozzle and accelerate the atomization, a time-varying disturbance with a small amplitude was added to the inlet velocity of the liquid jet (Zandian *et al.* 2019)

$$u_l(t) = U_l \left[1 + \gamma \sum_{i=1}^5 \sin \frac{2\pi U_l t}{(i+1)D} \right], \quad (4.1)$$

where γ is the amplitude factor with the setting value of 0.2%. The right side of the calculation domain is set as the free outflow boundary, and symmetry boundary conditions are applied to the other four sides. Liquid nitrogen (LN₂) is employed as the working liquid with a temperature equal to 97 K. Meanwhile, the initial surrounding gas is gaseous nitrogen (GN₂) with a temperature equal to 100 K. The main physical properties of the working fluids are shown in table 2. The adaptive mesh technology is used, and the minimum grid size length is 2.4 μ m.

It is noted that, in the following work, unless otherwise specified, the dimensionless time $t' = t/t^*$ is used. Here, t^* is the characteristic time, which can be determined by $t^* = L^*/U_0$; L^* is the characteristic length. Figure 14 shows the evolution of the surface profile and vortex structure (i.e. λ_2 isosurface) of the jet. The unstable Kelvin–Helmholtz waves are found to form at the beginning. They are characterized by a small amplitude, axisymmetric shape near the nozzle and the corresponding vortex structure is ring shaped. The foremost segment of the jet forms a mushroom-shaped tip, and droplets and ligaments continuously fall off the rim of the tip. As the jet develops, the unstable waves continue to grow under the action of aerodynamics, gradually deforming with 3-D characteristics and eventually forming multiple lobes. The vortex structure near the surface also undergoes similar deformations. Holes began to appear in the lobes, and droplets and liquid filaments broke off from the rims. Because many liquid fragments surround the liquid core, the atomization cone can be clearly observed. At the same time, numerous complex vortices are formed among the liquid column, ligaments and droplets, further aggravating the deformation and fragmentation of the jet.

4.2. Effect of phase change on the primary breakup

The evolution of the jet in an environment with a large temperature range was simulated to extensively investigate the effect of phase change on the primary breakup. Different

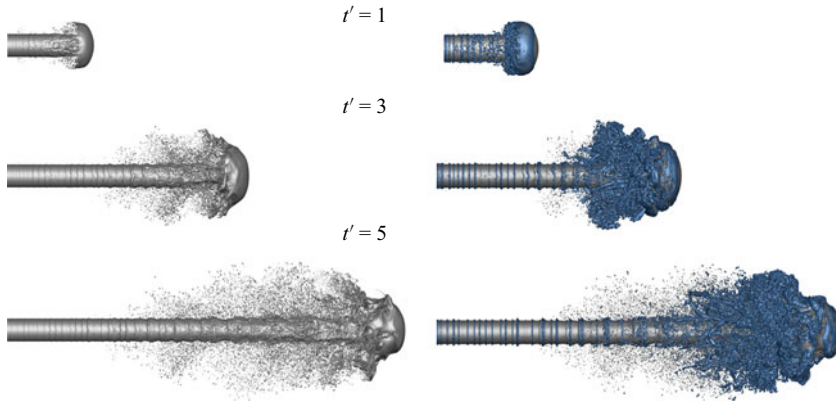


Figure 14. Evolution of jet morphology. The grey surface is the jet atomization morphology, and the blue surface is the vortex structure ($\lambda/2$ isosurface) near the jet.

environmental superheat degrees ($\Delta T_v = T_\infty - T_{sat}$) with 500 K, 1000 K and 1500 K are employed. Figure 15 shows the jet surface evolution at $t' = 5$ under different ΔT_v . It reveals that all jets have sequential structures of ring-mounted K-H unstable waves, 3-D K-H lobes and tips in the axial direction away from the nozzle outlet, accompanied by massive droplets and ligaments tapered around the liquid core. However, the quantity of droplets upstream significantly decreases with the increase of ΔT_v . This can be attributed to the fact that the droplets in this area are the first formed by the breakup of the tip, resulting in a longer thermal exposure in the environment. In the midstream of the jet, the quantity of droplets is also reduced to a certain extent, and the surface structure of the liquid core changes with the increase of ΔT_v , as shown in the local zoom on the right. According to Shinjo & Umemura (2010) and Zandian *et al.* (2019), the broken droplets hit the liquid core, and the vortex near the droplets acts on the jet surface. These are the main reasons for the breakup of the K-H lobe. Under the impact of numerous droplets and the complex vortices, the K-H lobe structure is destroyed, and the jet surface behaves irregularly during the simulation without phase change. With $\Delta T_v = 1500$ K, the K-H waves appearing at a certain frequency can still be observed, and the break occurs at the rim of the lobe although the surface is not smooth. Similar behaviours can also be observed in the corresponding vortex, as shown in the green box in figure 16. In this area, the gas flows over the droplets and a stretched strip-shaped vortex forms. The vortex of the non-vaporizing jet is omnidirectional. However, it tends to be consistent under high-temperature conditions, and the number of strip-shaped vortex structures increases with the increase of ΔT_v . Therefore, the flow field near the liquid core is relatively simple due to the reduction of droplets, which is also an important reason for the differences in the surface structures of the liquid core in figure 15.

The average volume distributions of broken droplets with various ΔT_v are compared in figure 17, where the grey dashed line represents the corresponding minimum cell volume. With no phase-change condition ($\Delta T_v = 0$), the droplet volume is normally distributed, and the mesh resolution can capture the droplets produced by the primary breakup. As ΔT_v increases, the volume distribution curve moves left, meaning that the quantity of large droplets decreases and the number of small droplets increases. This is mainly attributed to the reduction of the volume of all droplets caused by the occurrence of the phase change. The large droplets are highly unstable and prone to be deformed into liquid bags, sheets

Effect of phase change on jet atomization

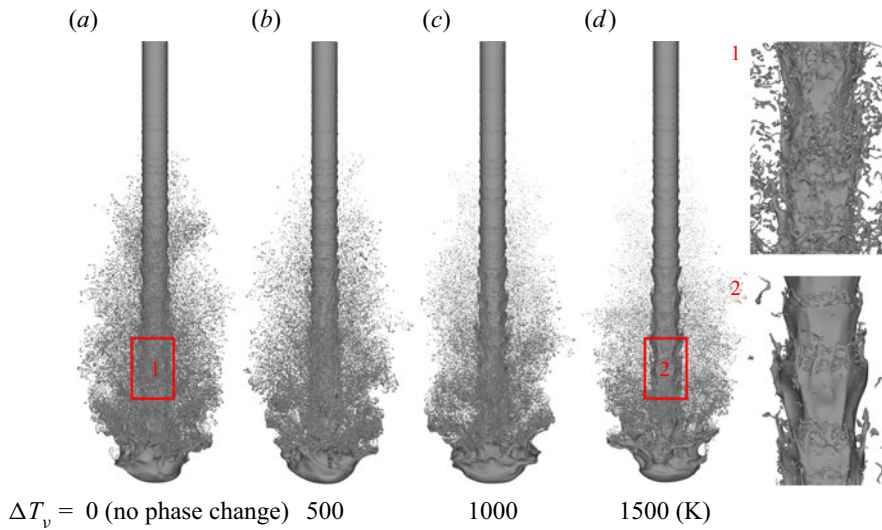


Figure 15. Jet morphology under different environmental superheat conditions at $t' = 5$. Images 1, 2 on the right are respectively local zoom of the jet surface with $\Delta T_v = 0$ and 1500 K. The cloud of tiny droplets near the jet has been deleted, and only the larger liquid structure is left.

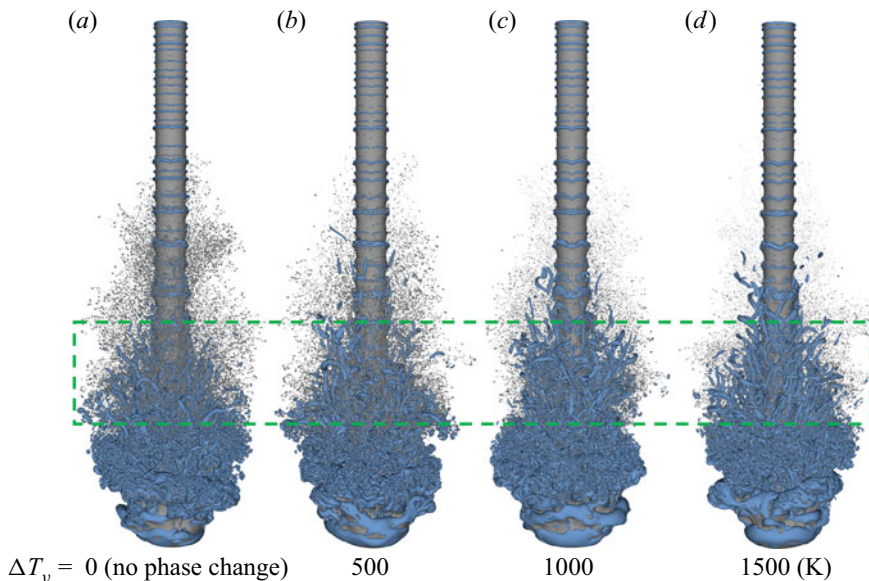


Figure 16. Vortex behaviour under different environmental superheat conditions at $t' = 5$. In the green box, the vapour flows over the droplets around the jet to form a large number of stretched strip-shaped vortex structures.

and ligaments. Take the sheet as an example, the air flows over the sheet to form a vortex, which will push the sheet to deform and thicken its rim. After breakup, the droplets formed by the rim are larger than those formed by the core. In a high-temperature environment, the vapour velocity near the rim is large, and the heat and mass transfers are more rapid. The sheet gets thinner and eventually breaks into smaller droplets. We discuss this in more detail in the section of secondary atomization this problem. Meanwhile, it seems that the

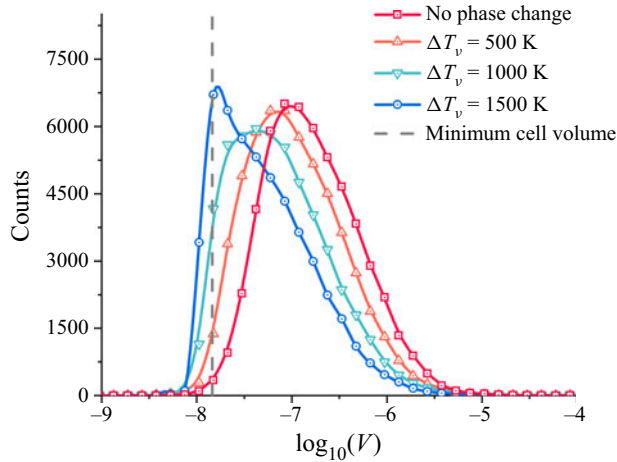


Figure 17. Droplet-volume distribution with no phase change and different superheat conditions at $t' = 5.5$. The grey dashed line is the volume corresponding to the smallest cell. In simulations, it is generally believed that the dynamic behaviour of droplets cannot be accurately described at scales smaller than the minimum cell volume.

total number of droplets also decreases. The curve of ΔT_v equal to 1500 K is steep on the left side of the minimum cell volume line because the grid resolution is not high enough to capture smaller droplets for this case. Considering that the variation trend of Sauter mean diameter (SMD) under phase change has been clarified and a finer grid will significantly increase the computational resource consumption, the current resolution is regarded as feasible for our requirements.

The droplet quantity distributions along the axial direction are further studied, as in figure 18. An obvious peak occurs on the curve without phase change at approximately $x=2$, which does not appear on the curve with $\Delta T_v = 1500$ K. In the middle and downstream, the deviation of the two curves becomes smaller, whereas the peak value of the curve with no phase change is slightly larger than the other. In general, the distribution curve at ΔT_v equal to 1500 K shows multiple peaks, indicating that the droplets fall off at a certain frequency. This is related to the K-H wave on the jet surface and the Rayleigh–Taylor (R-T) wave at the front end of the jet. When there is no phase change, the lobe structure is destroyed under the effect of a large number of droplets formed by breakage, as in figure 15 and the vortex in figure 16. It results in a variation in the droplet shedding frequency, and the curve only has peaks at the front and end. A detailed droplet-volume distribution at different locations along the axial direction is summarized in figure 19. It reveals that the case with no phase change presents normal droplet-volume distributions at different locations. In contrast, the peak of the droplet-volume distribution tends to move left close to the nozzle with $\Delta T_v = 1500$ K. This is consistent with the phenomenon observed from the jet morphology in figure 15, indicating that phase change obviously affects the spatial and volume distribution of droplets.

5. Phase change in secondary atomization

5.1. Droplet deformation and breakage without phase change

Compared with the primary breakup, the secondary atomization stage lasts longer; the movement morphology is more diverse, the coupling mechanism between phase change

Effect of phase change on jet atomization

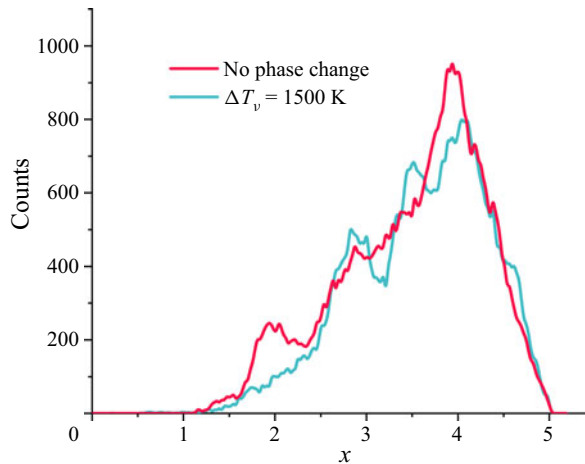


Figure 18. Distribution of droplet quantity along the axial direction at $t' = 5.5$. Here, x is a dimensionless parameter.

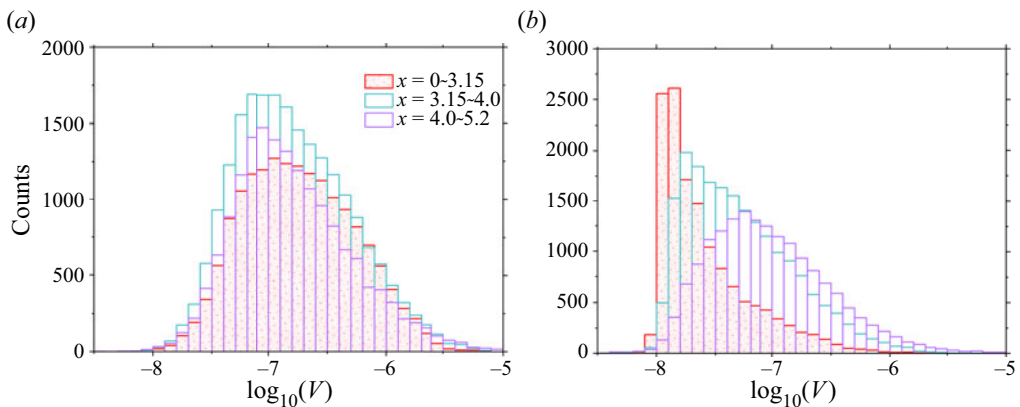


Figure 19. Axial volume distribution of droplets under different conditions at $t' = 5.5$. According to the axial distance from the entrance $x = 0-3.15$, $3.15-4.0$, $4.0-5.12$ (dimensionless parameters), the jet is divided into upstream, middle and downstream, respectively. And the local droplet-volume distributions in each part are shown. (a) No phase change and (b) $\Delta T_v = 1500$ K.

and droplet breakup is more complex. Hsiang & Faeth (1995) divided the atomization and the droplet deformation into different modes according to the We and Oh (ratio of viscous force to surface tension) numbers of the droplet, including deformation, oscillation, bag breakup, etc. (shown in figure 20). According to the droplet-volume distribution obtained by the primary breakup simulation of the jet, a droplet diameter equal to the peak value of the distribution curve is taken as the initial value $D_0 = 6 \mu\text{m}$ in the DNS of the droplet atomization. The main physical properties of the two phases are shown in table 2. The Oh number of the droplets is 0.0186 and the initial We numbers are set as 2.97, 9.63, 26.75, 74.3 and 199.85. As a result, the corresponding coordinate points are located in the five mode areas of deformation, oscillation deformation, bag breakup, multimode breakup and shear breakup mode in figure 20. The side length of the computational domain and the minimum cell size are set as $16.67D_0$ and $0.008D_0$, respectively. The surrounding boundary adopts the symmetry, and the top and bottom boundaries impose the outflow boundary condition.

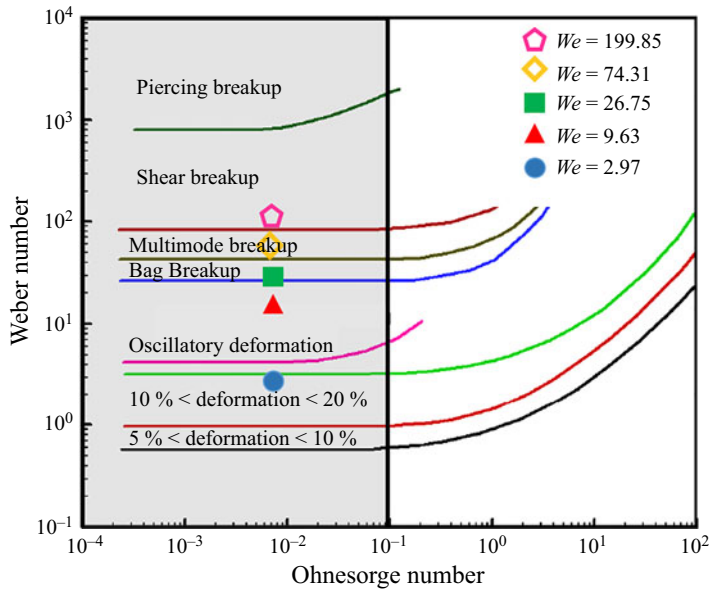


Figure 20. The We – Oh diagram of the secondary atomization mode. In the grey area where $Oh < 0.1$, the secondary atomization mode is only determined by We .

The numerical set-up is illustrated in detail in [figure 21](#), and this flow-field set-up is used in all secondary atomization simulations in § 5.

The morphology evolutions of droplet motion with various initial We numbers are shown in [figure 22](#). It reveals that the droplets only experience elastic deformation without breakage during the whole process at small We , as shown in [figures 22\(a\)](#) and [22\(b\)](#). As We increases, the droplet deformation amplitude increases and the morphological variation becomes more diverse. At large We numbers, as shown in [figure 22\(c–e\)](#), the large aerodynamic force against the surface tension means that the droplets are unable to rebound under the action of surface tension, leading to breakage. A typical bag break can be observed in [figure 22\(c\)](#). The bottom of the bag was first torn into a net shape and then broken into smaller droplets. Subsequently, an obvious Rayleigh–Plateau instability was formed on the rim, resulting in the generation of larger droplets. In the case shown in [figure 22\(d\)](#), the rim of the bag is continuously stretched and contracted inward to form a neck. The breakage first appears on the neck, followed by the bag core. The evolution of such a droplet morphology is very similar to the double-bag breakup observed by Cao *et al.* (2007) in their experiment. As We further increases in [figure 22\(e\)](#), the droplet deforms into a flat liquid sheet instead of a hemispherical bag. Droplets and ligaments are continuously broken off on the rim until the liquid sheet is completely fragmented. It is noted that a large We also leads to a more violent droplet breakage with a shorter breaking time and smaller droplet size. As We increases, the droplet atomization modes in [figure 22](#) are successively deformation, oscillation deformation, bag breakup, multimode breakup and shear breakup. It can be concluded that our simulation results are completely consistent with the predictions in the secondary atomization mode diagram from Hsiang & Faeth (1995) ([figure 20](#)). The simulation results are further compared with the experimental results by Dai & Faeth (2001). Dai & Faeth (2001) experimentally tested the secondary atomization of droplets in the range of $20 < We < 81$. The evolutions of the dimensionless maximum diameters obtained by experiments and simulations are

Effect of phase change on jet atomization

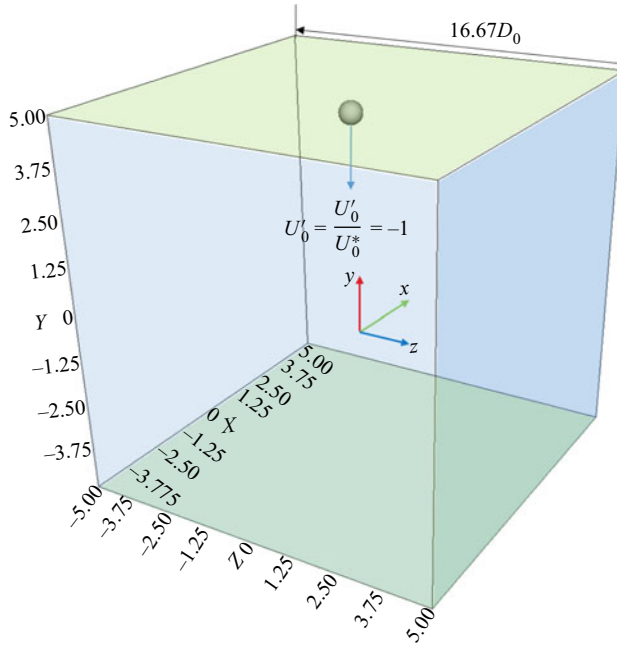


Figure 21. Schematic sketch of a droplet moving in stationary vapour. The computational domain is a cube with a side length of $16.67D_0$. In the simulation, physical parameters are processed without dimension. At the initial moment, the droplet velocity along the y -axis is -1 and the vapour velocity is zero. Setting the symmetry boundary conditions around the calculation domain (light blue filled), and the top and bottom surfaces as the outflow boundary (light green filled).

compared in [figure 23](#), which indicates that the numerical results with We equal to 26.75 and 74.03 show satisfactory coincidence with the experimental results.

5.2. Breakup performance of vaporizing droplets at high We

As mentioned above, the ISM is suitable for the violent breaking process of high We droplets. Assuming that the initial droplet is saturated, the initial environment temperature and the surrounding boundary temperature are kept consistent and Dirichlet boundary conditions are imposed at the gas–liquid interface $T_\Gamma = T_{sat}$ and computational domain boundary $T_w = T_v$.

The morphological evolution of droplet atomization with $We = 199.85$ and $\Delta T_v = 0$ K, 500 K is shown in [figure 24](#). Similar to the no phase-change case as in [figure 24\(a\)](#), droplet atomization stages from drop deformation, rim strip, neck breakup to sheet breakup are observed at $\Delta T_v = 500$ K, as shown in [figure 24\(b\)](#). No droplets are generated during the deformation stage, and then droplets begin to fall off the rim of the droplets under the action of aerodynamic shear. At the same time, the rim shrinks to the inner centre, forming a neck due to the effect of surface tension. The joint between the neck and the liquid sheet has the largest surface curvature, and holes appear here and the neck separates from the liquid sheet. Finally, the sheet continues to stretch and lose stability, and holes begin to appear. With the effect of the capillary force, they develop along the radial direction and coalesce with other holes, making the liquid sheet appear to be broken into a network.

However, the details of the broken form are different from those of the no phase-change case. It can be seen from the droplet shape in [figure 24\(a\)](#) that the bottom of the liquid

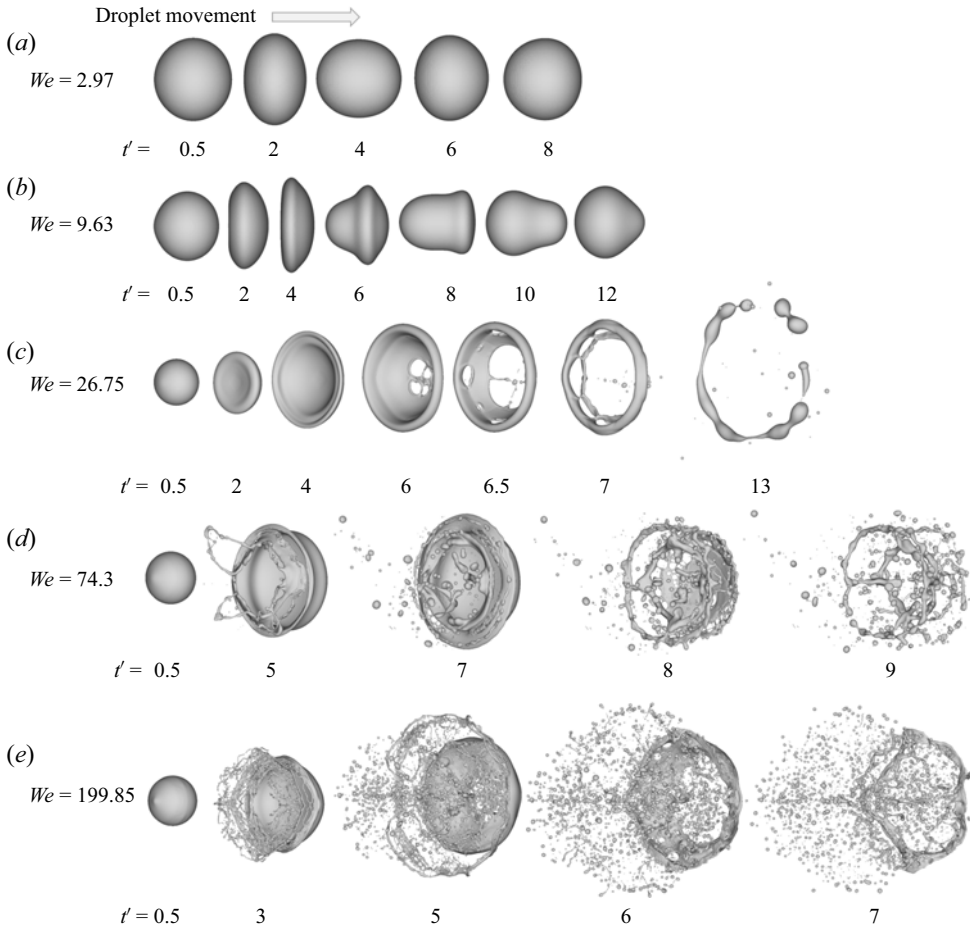


Figure 22. Deformation and fragmentation processes of droplets with different We . Here, t' is dimensionless time $t' = tU_0/L$. Note that U_0 is the droplet initial velocity, which is different in these five cases. Therefore, the corresponding dimensionless time scales are also different.

sheet is first broken under the impact of the tiny droplets, and breakup begins to spread to the surrounding rim. In contrast, the bottom and rim around break almost at the same time when phase change exists, as shown in figure 24(b) at $t' = 6$. The liquid being more evenly distributed in the core of the liquid sheet explains this phenomenon. Moreover, the results obtained after the completion of atomization at $t' = 7$ also indicate that the droplet atomization is more violent with $\Delta T_v = 500$ K.

To gain more insight, figure 25 shows the temperature and relative velocity distribution in the 2-D cross-section of the droplet at $t' = 5$. It is found that the gas temperature at the rear of the droplet is unevenly distributed. At the same time, a symmetrical vortex pair is formed by the airflow at the rear of droplet, as shown in figure 25(b). Recirculation by the vortex enhances the gas convection inside the droplet rim. As a result, phase change accelerates at the inner side of the edge, which quickly vaporizes the liquid accumulated here. It can be concluded that phase change changes the liquid distribution inside the sheet to a certain extent, also accounting for the difference in droplet atomization morphology.

Effect of phase change on jet atomization

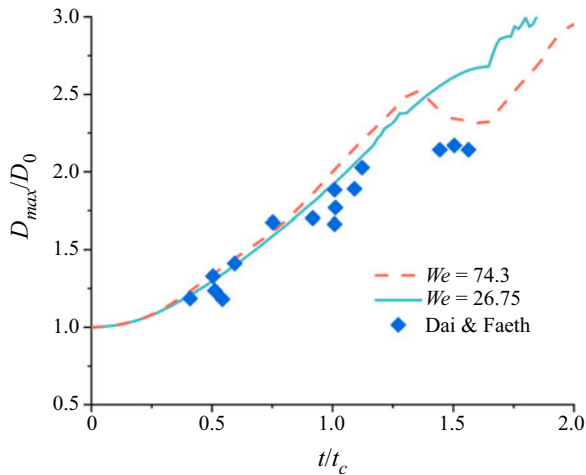


Figure 23. Variation in the maximum diameter of a droplet with time. Here, D_{max} is the maximum diameter of the droplet along the cross-stream, and the characteristic time $t_c = D_0(\rho_l/\rho_g)^{1/2}/U_0$.

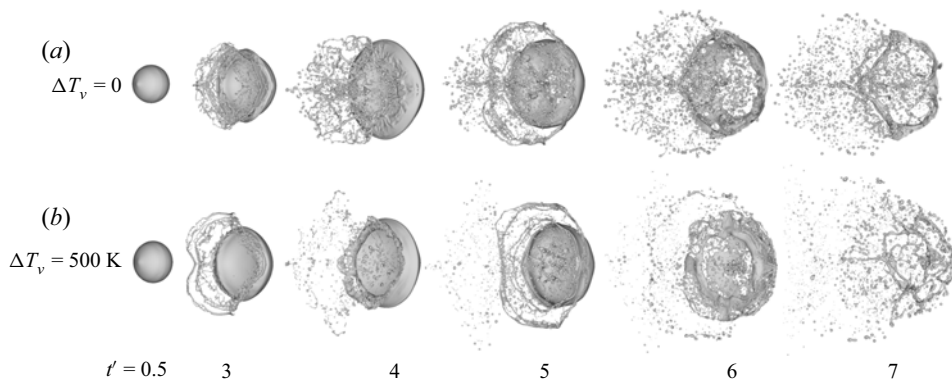


Figure 24. Morphology evolution of drop atomization. The typical characteristics of the droplet morphology development of $We = 199.85$ at several moments with $\Delta T_v = 0, 500$ K are shown in (a,b).

The growth of the total number of droplets during atomization is plotted in [figure 26](#). For most of the time during breakup, the counts of droplets without phase change is slightly higher than those with phase change. This is because extremely small droplets vaporize rapidly under high-temperature conditions. In addition, the three curves of the droplet count also shows a similar regularity, which reflects the development of morphology. Taking the case of no phase change as an example, the growth curve is divided into four stages according to the slope, as shown in [figure 26](#). In the rim strip and neck breakup stages, droplet shedding in a high-temperature environment lags behind the condition of no phase change. In the process of droplet deformation, the recirculating airflow on the back causes the liquid to accumulate at the rim. As the rim becomes thicker, the edge separates from the sheet, forming ligaments with the effect of capillary instability. Under the phase-change conditions, the vapour flow velocity inside and outside the rim is the largest, as shown in [figure 25\(b\)](#). This phenomenon strengthens the heat and mass transfer here and alleviates the accumulation of liquid. Finally, in the sheet breakup stage,

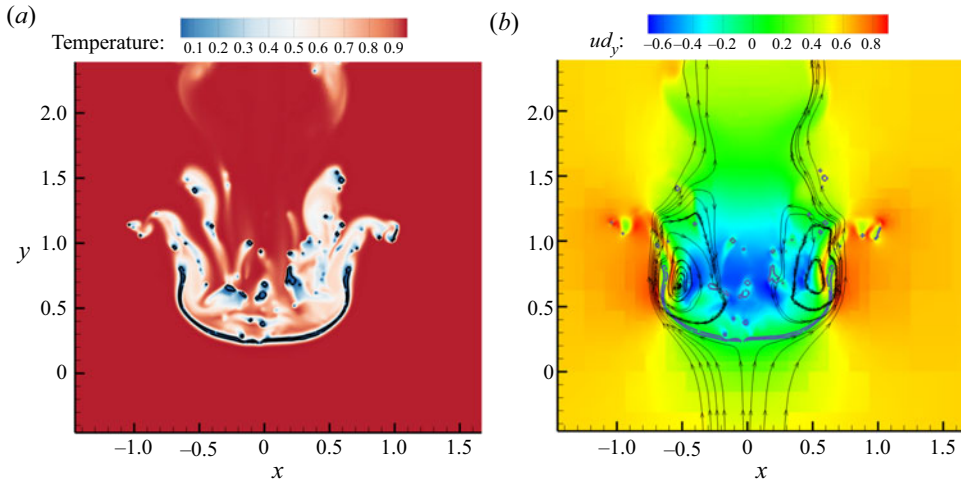


Figure 25. (a) Temperature field near the droplet of case $We = 199.85$, $\Delta T_v = 500$ K, at $t' = 5$. The black solid line is the gas–liquid interface. The temperature is a dimensionless parameter processed by $(T - T_s)/(T_v - T_s)$. (b) Relative velocity distribution and streamline diagram. Here, ud_y is dimensionless velocity along the flow direction $ud_y = U'_y - U'_{y,stag}$, where $U'_{y,stag}$ is the velocity at the stagnation point below the droplet.

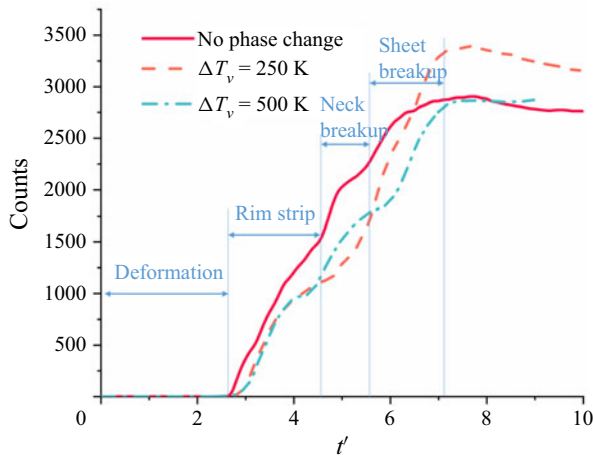


Figure 26. Counts of droplet changes during secondary atomization for different superheat conditions with $We = 199.85$. According to the slope, the blue lines, arrows and text divide the four stages of the no phase-change case, corresponding to the droplet-breakup stages including deformation, rim strip, neck breakup and sheet breakup. The other two curves can also be divided like this.

the droplet number increase is significantly faster than that without phase change. At $\Delta T_v = 250$ K, phase change makes the sheet stretch more uniformly and break more completely, leading to droplet counts higher than the result without phase change. But the effect of violent vaporization prevails as ΔT_v increases to 500 K, and the final droplet counts decrease instead.

Figure 27 shows the corresponding volume distribution of atomized droplets with various gas superheats. Two peaks appear on the droplet-size distribution curve without phase change, and the right peak gradually disappears on the curves as ΔT_v grows. This is probably due to the thicker rim of the liquid sheet. The breakup of the rim lags behind

Effect of phase change on jet atomization

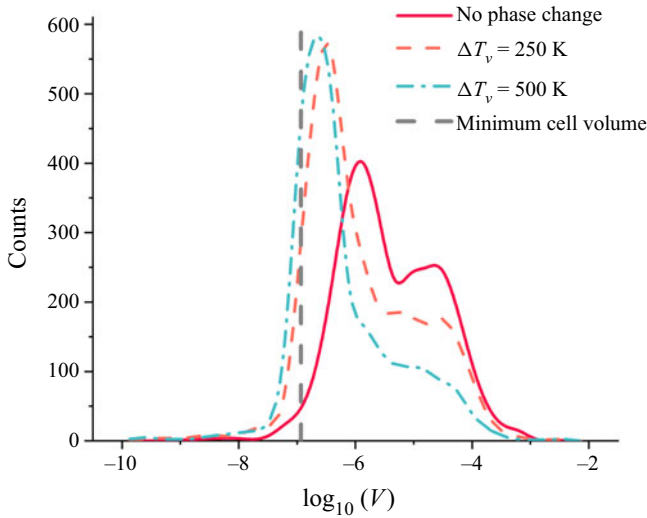


Figure 27. Volume distribution of atomized droplets of $We = 199$ under different superheat conditions at $t' = 8$. The grey dashed line is the volume corresponding to the smallest cell.

the breakage of the liquid sheet, and the size of the droplets produced is slightly larger. However, the occurrence of phase change improves this phenomenon by making the liquid distribution inside the liquid sheet uniform and reducing the volume of the large droplet. Moreover, the droplet-volume distribution peak shifts to the left as the environmental superheat increases; the droplet size is concentrated at the corresponding volume of the minimum cell. The main reasons are that the phase change reduces the volume of all droplets, and the fragmentation of the liquid sheet produces more droplets with smaller volumes.

5.3. Breakup performance of the moving vaporizing droplets at low We

The DNS modelling of the droplet deformation with small We is carried out with STDM. The numerical set-up is the same as §§ 5.1 and 5.2. Figure 28 shows the movement and deformation of the droplet with ΔT_v and We equal to 500 K and 9.63, respectively. It reveals that the droplet deformation behaviour at some stages shows a significant difference from the case without phase change in figure 28(a). For example, the front edge of the droplet is almost flat at $t' = 4$ in figure 28(b) and it is disc shaped in figure 28(a) without phase change. Afterward, the droplet rebounds and bulges upward and becomes a semi-ellipse at $t' = 6$, instead of a flying-saucer shape as in figure 28(a).

To clarify the reason for the abovementioned difference, the drag coefficient is employed to analyse gas flow resistance against the droplet. The unsteady drag coefficient (Shao *et al.* 2017) (5.1) is calculated from the deformation and velocity variation of the droplet

$$C_D = \frac{\rho_l V \frac{dU_r}{dt}}{\frac{1}{2} \rho_v U_r^2 A_{front}}, \quad (5.1)$$

where V and A_{front} are the liquid volume and frontal area, respectively; A_{front} can be obtained from $A_{front} = \pi(D_{max}/2)^2$; U_r is the relative velocity and defined as $U_r = U_l - U_v$.

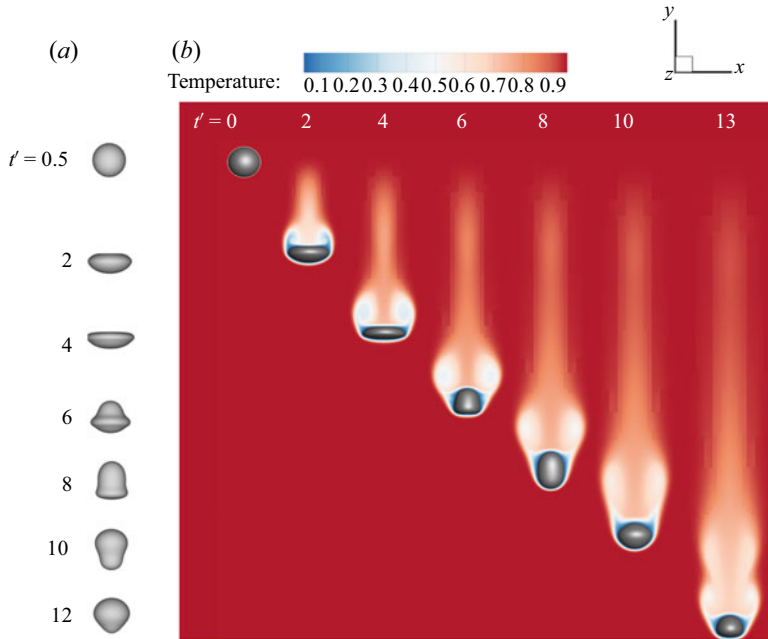


Figure 28. Droplet morphology evolution of $We = 9.63$. (a) Without phase change. (b) With the condition of $\Delta T_v = 500$ K. Figure shows the dimensionless temperature contour at different moments. The symmetrical vortex pair caused by recirculation can be observed.

The variation trend of Re and We during the movement of the droplet is shown in [figure 29](#). Under the effect of aerodynamic resistance, both Re and We related to the velocity gradually decrease and fluctuate with the deformation of the droplet. With the increase of environmental superheat, the droplet deceleration effect becomes more obvious. The decrease in the inertial force introduced by deceleration means that the surface tension gradually dominates the deformation. The droplet rebounds quickly once it deviates from the equilibrium state, which explains that the droplet's deformation amplitude decreases with the increase of temperature. Consequently, the variation of C_D can be obtained according to (5.1) with various ΔT_v , as in [figure 30](#). This illustrates that C_D rapidly decreases initially when Re decreases, which is attributed to the impulsive acceleration of droplet in a stationary gas reported by Wadhwa, Magi & Abraham (2007). Then, C_D experiences a slow decrease stage as Re gradually decreases. Obvious fluctuations appear at Re approximately equal to 600. This is related to the deformation of the droplet and the fluctuation of the droplet acceleration. Besides, C_D increases with the growth of ΔT_v , indicating that the droplet suffers more aerodynamic resistance when travelling in a higher-temperature environment.

When the gas–liquid interface undergoes phase change, a typical flow feature is the velocity jump across the interface along the normal direction, which is produced by the volume expansion in the gas phase, also known as Stefan flow. The streamline diagrams of the droplets without and with phase change are depicted in [figures 31\(a\)](#) and [31\(b\)](#), respectively. The stagnation point below the droplet is taken as the reference system. The streamlines closely adhere to the surface of the droplet and flow around without phase change, as shown in the red circle in [figure 31\(a\)](#). In contrast, the gas streamlines nearly below the droplet do not adjoin the interface in [figure 31\(b\)](#). The streamline that goes from

Effect of phase change on jet atomization

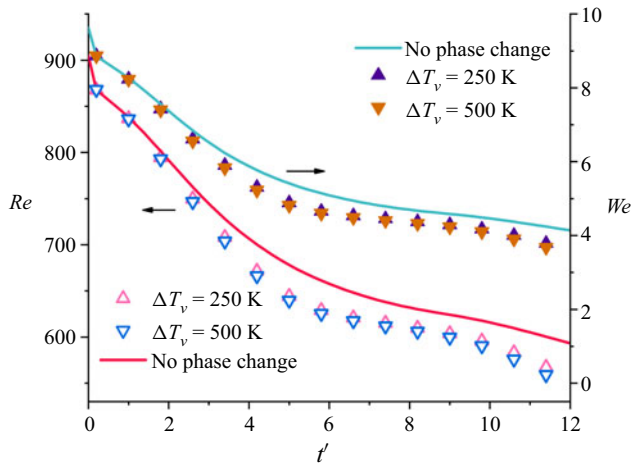


Figure 29. Variation trends of Re and We during droplet movement. The y-axis on the left is Re , and the right is We . The solid red line and the coloured hollow dots represent the changes of Re over the dimensionless time under different superheat conditions. The green solid line and the coloured solid dots represent the variation in We .

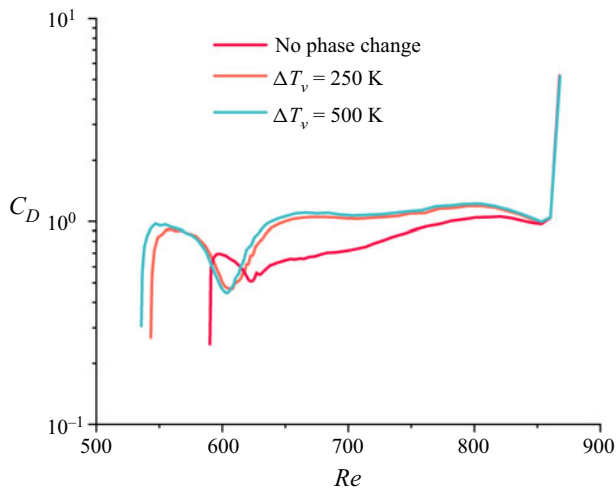


Figure 30. Variation in C_D during droplet movement under different superheat conditions. Here, Re will gradually decrease as the droplet advances. Therefore, curves from right to left in the figure are the evolution of C_D during the droplet movement.

the droplet surface into the vapour indicates the appearance of Stefan flow. Consequently, the near region of the interface can be treated as a vapour interlayer. Figure 31(c) shows the temperature distribution (in the form of isolines) and the mass source term distribution (in the form of contours) near the vaporizing droplet. The temperature boundary layer is thinner upwind of the droplet, resulting in a significantly larger temperature gradient than at other positions, and thus a larger corresponding mass source term. It can be understood that the heat and mass transfers on the droplet surface are not uniform during the movement, and they impact the velocity field in the form of Stefan flow in reverse. The difference in vapour velocity above and below the droplet provides a buffer for the

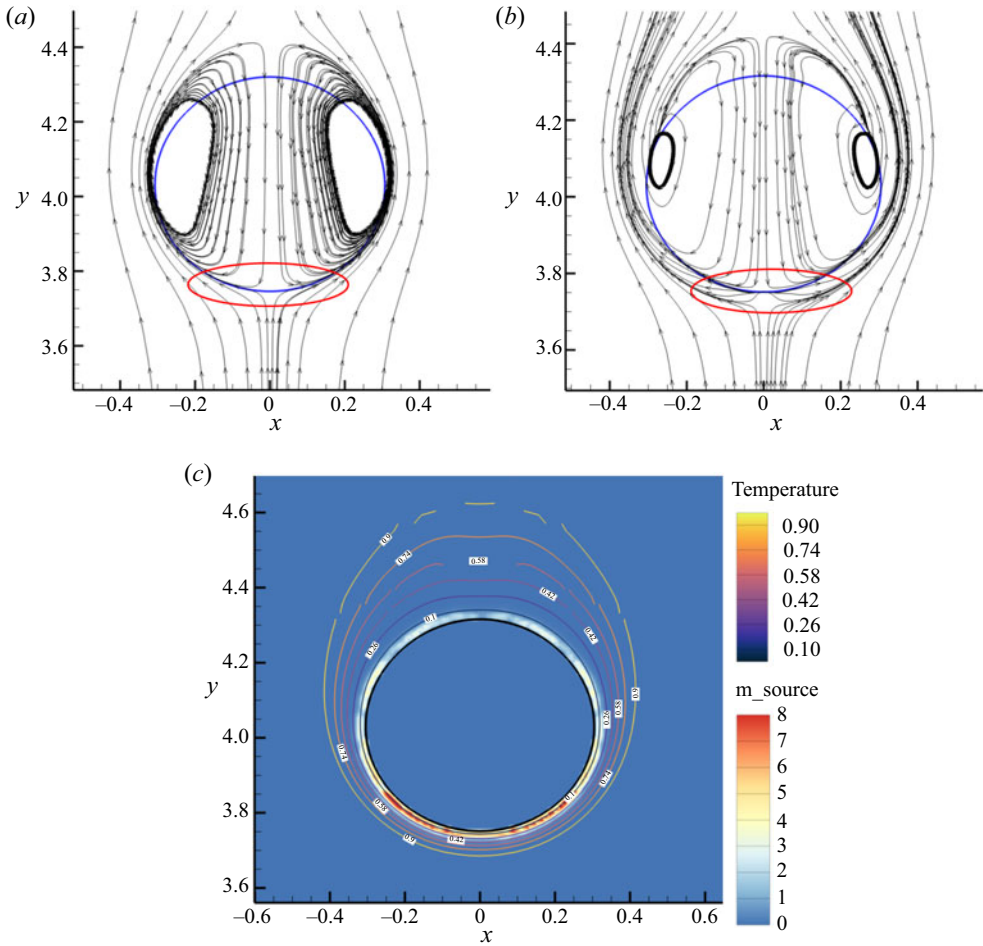


Figure 31. (a) Streamline diagram at $t' = 0.5$ without phase change. The solid blue line is the gas–liquid interface. The streamlines of the vapour below the droplet are shown by the red circle. (b) Streamline diagram at $t' = 0.5$ with $\Delta T_v = 500$ K. (c) Temperature and mass source term distribution near the droplet with $\Delta T_v = 500$ K at $t' = 0.5$. The coloured line represents the temperature isolines, and the fill colour represents the contour of the mass source term.

movement of the droplets, which is an important reason for the increase of the aerodynamic resistance on the droplet (described by the drag coefficient) and the subsequent decrease of droplet deformation.

5.4. Phase-change rate for various We

Phase-change rates for various We are further investigated. The variation of the droplet equivalent diameter converted from the remaining volume of the droplet is plotted in figure 32. The characteristic time t^* in figure 32 is unified as $t^* = L^*/U_0$, where U_0 is equal to 10 m s^{-1} . With the increase of We , the equivalent droplet diameter decreases with acceleration. A local zoom of the beginning of the cases with large We reveals that the two curves experience slow followed by fast variation.

Accordingly, phase-change rates can be obtained from the variation of the droplet equivalent diameter as in figure 33. It is seen that the phase-change rate significantly

Effect of phase change on jet atomization

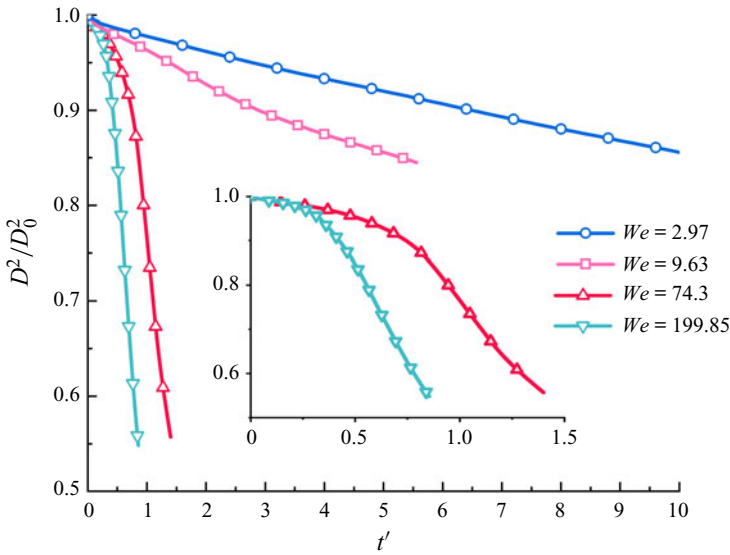


Figure 32. Variation of droplet equivalent diameter with dimensionless time at $\Delta T_v = 500$ K of different We . Considering that the time scales of several cases are significantly different, two large We cases are shown independently.

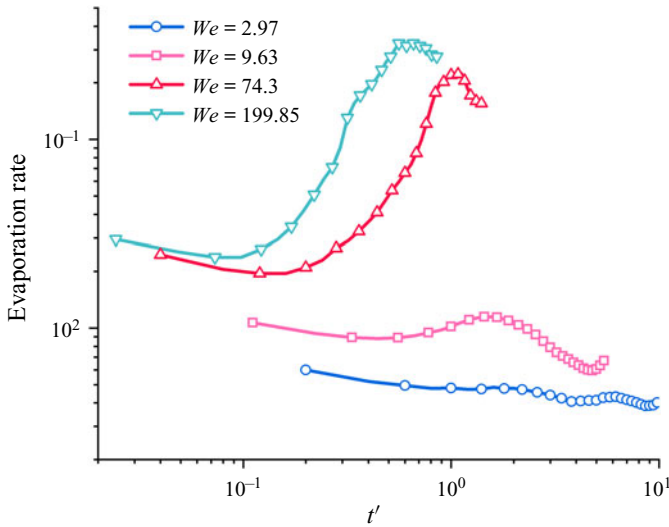


Figure 33. Variation of droplet-volume phase-change rates with dimensionless time at $\Delta T_v = 500$ K for different We . The discretized phase-change rate can be calculated by $(V_d^{n+1} - V_d^n)/\Delta t$, where V_d is the remaining volume of the droplet.

increases with the increase of We . Moreover, curves are varied smoothly with small We . The occurrence of deceleration and deformation is attributed to the curve variation. Once droplet breakup happens ($We = 74.3$ and 199.85), the phase-change rate varies drastically.

6. Conclusions

In this study, DNS investigations were carried out on primary breakup and secondary atomization with phase change. For the primary breakup and secondary atomization with high We , the ISM was employed as the phase-change numerical method. For the secondary atomization with low We , we built the STDM to deal with the phase change across the interface. Subsequently, the effect of phase change on the characteristics of jet atomization was evaluated, such as the morphology and atomized droplet-volume distribution. The main conclusions are as follows:

- (i) The established STDM can accurately capture the velocity evolution at the interface, and it performs better than the existing ISM.
- (ii) The application of the STDM in violent atomization is limited by the high computational resource consumption, and it is suitable for the deformation modelling of droplets with low We . The ISM is easy to implement, which is suitable for primary crushing and high We secondary atomization.
- (iii) The phase change affects some details in the primary breakup, such as the jet surface morphology, droplet distribution and size.
- (iv) The phase change makes the droplet break more completely at high We , while it increases the resistance of droplets at low We .
- (v) Phase -change rate increases with increasing We in secondary atomization.

Supplemental movies. Supplementary movies are available at <https://doi.org/10.1017/jfm.2021.1158>.

Funding. The authors greatly acknowledge the support from the National Natural Science Foundation of China (No. 51806069). The computing work in this paper is supported by the public computing service platform provided by the Network and Computing Center of HUST.

Declaration of interests. The authors report no conflict of interest.

Author ORCIDs.

 Jianye Chen <http://orcid.org/0000-0002-4185-4278>.

Appendix A. Description of numerical methods

A.1. Interface shift method

The ISM calculates the interface shift velocity based on mass and energy conservation. By superimposing \mathbf{u}_I with the original velocity field, it solves the VOF convection equation, and then restores the velocity field

$$\mathbf{u}_I = \frac{((\lambda \nabla T)_l - (\lambda \nabla T)_v) \cdot \mathbf{n}}{\rho_l h_{fg}}. \quad (\text{A1})$$

Considering that the calculation of the interface displacement velocity requires an accurate solution of the temperature field, a correction source term is added to the energy equation in the mixing cells to apply the Dirichlet boundary condition at the interface, ensuring that the interface temperature remains saturated

$$\partial_t T = \nabla \cdot (\alpha \nabla T) - \frac{T - T_{sat}}{\tau_c} \delta_S(x_1), \quad (\text{A2})$$

where τ_c is the control time and it is taken as $\tau_c = 10$.

Effect of phase change on jet atomization

The temperature gradient at the interface is approximated by weighing the temperature gradient of both vapour and liquid grids adjacent to the interface. Taking the 2-D case as an example

$$\partial_x T \approx n_x^2 \partial_x T \left(x + \frac{\Delta}{2}, y \right) + n_y^2 \partial_x T \left(x + \frac{\Delta}{2}, y + \Delta \right), \quad (\text{A3})$$

where n_x and n_y are the x -direction and y -direction components of the interface normal vector, respectively, and Δ is the side length of the grid.

A.2. Source diffusion

The main practical steps are summarized as follows:

Step 1:

Integrate the mass source term in the entire computational domain to calculate the total mass flow of the phase interface

$$\dot{m}_{int} \iiint_V \ddot{m} dV. \quad (\text{A4})$$

Step 2:

Obtain the diffusion of volume source field by solving a diffusion equation as follows:

$$\ddot{m}_1 - \nabla \cdot [(D\Delta\tau)\nabla\ddot{m}_1] = \dot{m}_0, \quad (\text{A5})$$

where D is the diffusion coefficient used to control the thickness of the source term layer, and it is directly proportional to the square root of the product of diffusion constant and artificial time step $((D\Delta\tau)^{1/2})$. The value of the diffusion coefficient is determined from the grid resolution; usually, the source term layer thickness should be controlled within a few layers of grids.

Step 3:

Set the value of the mass source term in the mixing cells to 0, whose volume fraction is located between 0 and 1 ($0 < f < 1$) in the VOF method. To ensure the mixing cells are not affected by the mass source term in the calculation and to ensure continuity of velocity at the interface, the value of mass source term in the mixing cells is set to 0.

Step 4:

The source field on both sides of the interface is proportionally scaled to ensure the conservation of mass. The scale factor can be obtained by dividing the total mass flow rate of the interface by the integral of the source field on both sides of interface

$$N_l = \dot{m}_{int} \left\{ \iiint_V [H_l(f - 0.5)\ddot{m}_1 dV] \right\}^{-1}, \quad (\text{A6})$$

$$N_v = \dot{m}_{int} \left\{ \iiint_V [H_v(0.5 - f)\ddot{m}_1 dV] \right\}^{-1}. \quad (\text{A7})$$

Here, H is the Heaviside function, and the computational domain is divided into a gas-phase domain and a liquid-phase domain with $f = 0.5$ as the boundary.

Finally, multiply the mass source terms in the gas and liquid phases by the scale factor to obtain the final source term field

$$\ddot{m} = N_v H_v(0.5 - f)\ddot{m}_1 - N_l H_l(f - 0.5)\ddot{m}_1. \quad (\text{A8})$$

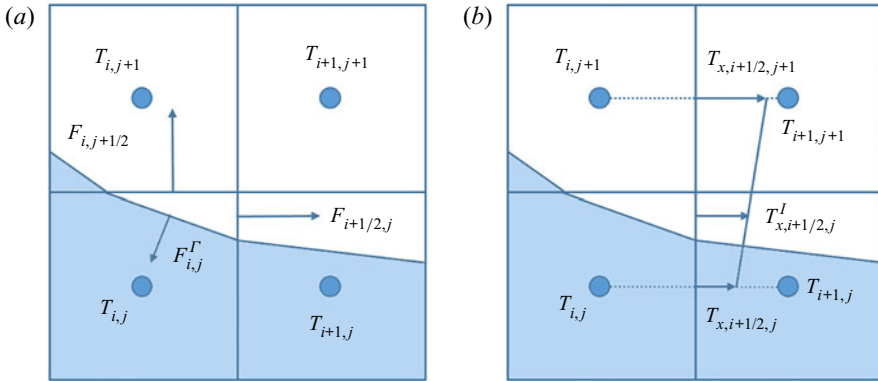


Figure 34. Schematic diagram of (a) the control volume formulation based on the divergence of appropriately centred fluxes, (b) technique of obtaining a properly centred normal derivative by interpolating between two neighbouring values.

A.3. Embed boundary method

Taking the phase represented by $f = 1$ as an example, the discretization format of the grid containing the interface as shown in figure 34 can be expressed as follows:

$$\alpha \nabla \cdot \nabla T = \frac{\alpha}{\Delta x \Delta y f_{i,j}} (F_{i+1/2,j} - F_{i-1/2,j} + F_{i,j+1/2} - F_{i,j-1/2} - F_{i,j}^\Gamma), \quad (\text{A9})$$

where $\alpha = \lambda / \rho c_p$ is the thermal diffusivity; Δx and Δy are the length and width of the grid, respectively. The subscripts i and j represent the grid label. As in figure 34(a), F is the centred diffusion flux through each surface, and $F_{i,j}^\Gamma$ is the centred diffusion flux through the phase interface. It should be noted that, for the face that intersects with the phase interface, its central flux needs to be calculated by interpolating between two neighbouring values, as shown in figure 34(b).

Taking the left face of the cells as an example, the diffusion flux across the face can be obtained as follows:

$$F_{i+1/2,j} = a \Delta y \alpha \left[\frac{(1+a)(T_{i+1,j} - T_{i,j})}{2 \Delta x} + \frac{(1-a)(T_{i+1,j+1} - T_{i,j+1})}{2 \Delta x} \right], \quad (\text{A10})$$

where a is the face fraction of the mixing cell. All the faces use the gradient values corresponding to the centre of the face. Therefore, the gradient value should be obtained by linear interpolation for the face with a ranging from 0 to 1. When $a = 1$, (A10) degenerates to a common central difference scheme.

The diffusion flux on the phase interface is determined according to the normal gradient formula (A11)

$$F^f = \alpha A^f \frac{\partial T}{\partial n}, \quad (\text{A11})$$

where A^f is the area of phase interface in the mixing cell.

Appendix B. Description of test cases

B.1. Mesh resolution

The mesh resolution level and the corresponding minimum grid size are given in table 3.

Cases	Level	Minimum mesh size (mm)
Droplet deformation Stefan problem	11	0.0179 ($D_0/128$)
	6	0.156
	7	0.078
	8	0.039
Bubble growth	8	0.156
	9	0.078
	10	0.039
Single drop phase change	8	0.313

Table 3. Grid resolution level and minimum grid size of different cases.

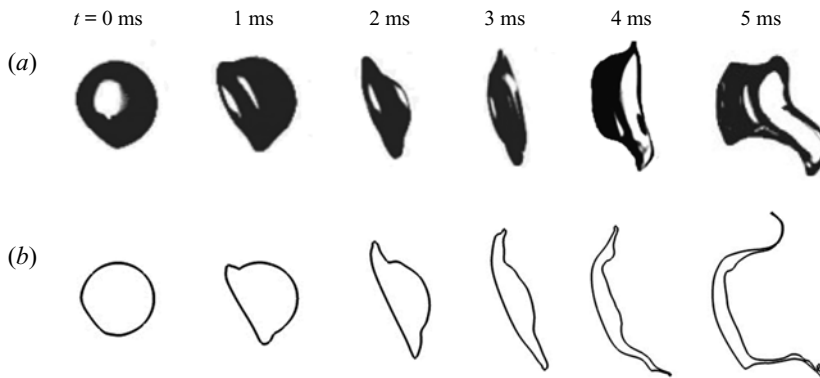


Figure 35. (a) Droplet morphology evolution in experiment. (b) Numerical results in present work.

B.2. Validation of droplet deformation and trajectory

The secondary breakup experiment with an ethyl alcohol droplet by Flock *et al.* (2012), which has been widely used in the validation of numerical simulations (Tavangar, Hashemabadi & Saberimoghdam 2015; Yang *et al.* 2016; Wang & Yang 2019), is employed to validate the accuracy of the present numerical method. In their experiment, the deformation and fragmentation of a single ethanol droplet injected into a continuous air jet were investigated using high-speed shadowgraphy and the particle image velocimetry method. The case of $We = 32$, $Re_g = 2500$, $Oh = 0.0059$ is simulated with gravity. Figure 35 shows the comparison between the simulation results and experimental results at different moments. It reveals that the droplet morphology evolution in the current numerical simulation is in satisfactory agreement with the experimental image. Moreover, the numerical droplet motion trajectory is compared with the experimental average value in figure 36. The error is negligible compared with the experimental trajectory, although there is a slight deviation in the early stage since the initial x -direction velocity of the droplet is 0 in the numerical simulation. Therefore, it can be concluded that the numerical method used in this paper can well predict the development of the droplet trajectory and morphology.

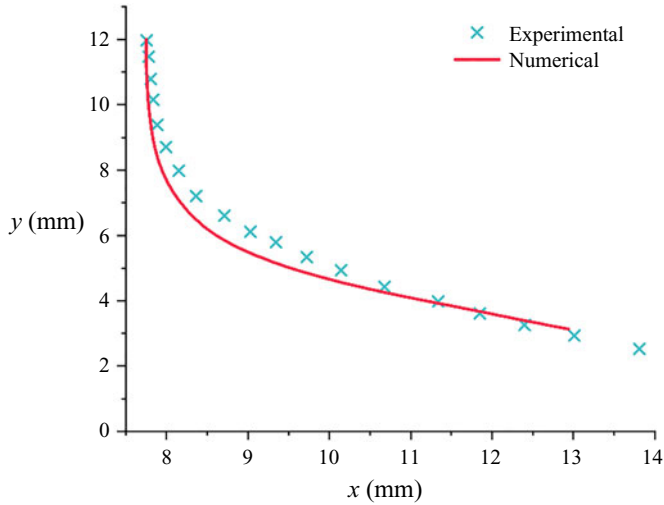


Figure 36. Comparison between the numerical and experimental droplet trajectories.

B.3. Stefan problem

Assuming a linear distribution of the gas-phase temperature, the analytical solution of the interface position can be obtained according to Welch & Wilson (2000)

$$\delta(t) = 2\vartheta\sqrt{\alpha t}. \tag{B1}$$

Here, δ is the thickness of vapour layer, and ϑ is the growth constant, which can be obtained by solving the following transcendental equation:

$$\vartheta \exp(\vartheta^2) \operatorname{erf}(\vartheta) = \frac{c_{p,g} T_{sup}}{h_{fg} \sqrt{\pi}}. \tag{B2}$$

B.4. Bubble growth under no gravity

The analytical solution of bubble radius varies with time as follows:

$$R = 2\beta_g \sqrt{\frac{\lambda_l}{c_{pl}\rho_l} t}, \tag{B3}$$

where β_g is the growth constant, which can be obtained from the following formulation:

$$\begin{aligned} & \frac{\rho_l c_{pl} (T_\infty - T_{sat})}{\rho_g (h_{fg} + (c_{pl} - c_{pg})(T_\infty - T_{sat}))} \\ &= 2\beta_g^2 \int_0^1 \exp\left(-\beta_g^2 \left((1-\zeta)^{-2} - 2\left(1 - \frac{\rho_g}{\rho_l}\right)\zeta - 1 \right)\right) d\zeta, \end{aligned} \tag{B4}$$

where ζ is the dummy variable of integration. The analytical solution for the evolution of temperature distribution along the radial direction with time can be expressed as

follows:

$$T = \begin{cases} T_{\infty} - 2\beta_g^2 \left(\frac{\rho_v(h_{fg} + (c_{pl} - c_{pg})(T_{\infty} - T_{sat}))}{\rho_l c_{pl}} \right) \\ \times \int_{1-R/r}^1 \exp \left(-\beta_g^2 \left((1 - \zeta)^{-2} - 2 \left(1 - \frac{\rho_g}{\rho_l} \right) \zeta - 1 \right) \right) d\zeta & \text{for } r > R. \\ T_{sat} & \text{for } r \leq R. \end{cases} \quad (\text{B5})$$

B.5. Phase change of a single drop in a quiescent gas environment

For the simulation using a virtual working fluid, its basic physical properties are as follows: liquid density $\rho_l = 200 \text{ kg m}^{-3}$; viscosity $\mu_l = 0.1 \text{ Pa s}$; heat capacity $C_{pl} = 400 \text{ J (kg K)}^{-1}$; thermal conductivity $\lambda_l = 40 \text{ W (m K)}^{-1}$; gas density $\rho_g = 5 \text{ kg m}^{-3}$; viscosity $\mu_g = 0.005 \text{ Pa s}$; heat capacity $C_{pg} = 200 \text{ J (kg K)}^{-1}$; thermal conductivity $\lambda_g = 1 \text{ W (m K)}^{-1}$; surface tension coefficient $\sigma = 0.1 \text{ N m}^{-1}$; latent heat coefficient $h_{fg} = 10\,000 \text{ J kg}^{-1}$; and saturation temperature $T_{sat} = 0 \text{ K}$. Chai *et al.* (2018) obtained an analytical solution for the mass flow rate (B6) of the droplet vaporization and the variation of the droplet diameter (B7) by assuming that the temperature from the gas–liquid interface to the boundary of the computational domain is linearly distributed

$$\dot{m} = \frac{2\lambda_g}{h_{fg}} \frac{T_{bc} - T_{sat}}{L - d}, \quad (\text{B6})$$

$$d = L - \sqrt{(L - d_0)^2 + \frac{8\lambda_g}{\rho_l h_{fg}} (T_{bc} - T_{sat})t}. \quad (\text{B7})$$

REFERENCES

- AGARWAL, A. & TRUJILLO, M.F. 2018 A closer look at linear stability theory in modeling spray atomization. *Intl J. Multiphase Flow* **109**, 1–13.
- ANEZ, J., AHMED, A., HECHT, N., DURET, B., REVEILLON, J. & DEMOULIN, F.X. 2019 Eulerian–Lagrangian spray atomization model coupled with interface capturing method for diesel injectors. *Intl J. Multiphase Flow* **113**, 325–342.
- AULISA, E., MANSERVISI, S., SCARDOVELLI, R. & ZALESKI, S. 2007 Interface reconstruction with least-squares fit and split advection in three-dimensional Cartesian geometry. *J. Comput. Phys.* **225**, 2301–2319.
- CAO, X., SUN, Z., LI, W., LIU, H. & YU, Z. 2007 A new breakup regime of liquid drops identified in a continuous and uniform air jet flow. *Phys. Fluids* **19**, 057103.
- CHAI, M., LUO, K., SHAO, C., WANG, H. & FAN, J. 2018 A coupled vaporization model based on temperature/species gradients for detailed numerical simulations using conservative level set method. *Intl J. Heat Mass Transfer* **127**, 743–760.
- DAI, Z. & FAETH, G.M. 2001 Temporal properties of secondary drop breakup in the multimode breakup regime. *Intl J. Multiphase Flow* **27**, 217–236.
- FLOCK, A.K., GUILDENBECHER, D.R., CHEN, J., SOJKA, P.E. & BAUER, H.J. 2012 Experimental statistics of droplet trajectory and air flow during aerodynamic fragmentation of liquid drops. *Intl J. Multiphase Flow* **47**, 37–49.
- FUSTER, D., BAGUÉ, A., BOECK, T., LE MOYNE, L., LEBOSSETIER, A., POPINET, S., RAY, P., SCARDOVELLI, R. & ZALESKI, S. 2009 Simulation of primary atomization with an octree adaptive mesh refinement and VOF method. *Intl J. Multiphase Flow* **35**, 550–565.
- GEORGIOULAS, A., ANDREDAKI, M. & MARENGO, M. 2017 An enhanced VOF method coupled with heat transfer and phase change to characterise bubble detachment in saturated pool boiling. *Energies* **10**, 272.

- GIBOU, F., CHEN, L., NGUYEN, D. & BANERJEE, S. 2007 A level set based sharp interface method for the multiphase incompressible Navier–Stokes equations with phase change. *J. Comput. Phys.* **222**, 536–555.
- GORDILLO, J.M., PÉREZ-SABORID, M. & GAÑÁN-CALVO, A.M. 2001 Linear stability of co-flowing liquid–gas jets. *J. Fluid Mech.* **448**, 23–51.
- HARDT, S. & WONDRA, F. 2008 Evaporation model for interfacial flows based on a continuum-field representation of the source terms. *J. Comput. Phys.* **227**, 5871–5895.
- HEINDEL, T.T. 2018 X-ray imaging techniques to quantify spray characteristics in the near field. *Atom. Spray* **28**, 1029–1059.
- HERRMANN, M. 2011 On simulating primary atomization using the refined level set grid method. *Atom. Spray* **21**, 283–301.
- HOYAS, S., GIL, A., MARGOT, X., KHUONG-ANH, D. & RAVET, F. 2013 Evaluation of the Eulerian–Lagrangian Spray Atomization (ELSA) model in spray simulations: 2D cases. *Math. Comput. Model.* **57**, 1686–1693.
- HSIANG, L.P. & FAETH, G.M. 1995 Drop deformation and breakup due to shock wave and steady disturbances. *Intl J. Multiphase Flow* **21**, 545–560.
- HUANG, J. & ZHAO, X. 2019 Numerical simulations of atomization and evaporation in liquid jet flows. *Intl J. Multiphase Flow* **119**, 180–193.
- IBRAHIM, E.A., YANG, H.Q. & PRZEKWAŚ, A.J. 1993 Modeling of spray droplets deformation and breakup. *J. Propul. Power* **9**, 651–654.
- JAIN, S.S., TYAGI, N., PRAKASH, R.S., RAVIKRISHNA, R.V. & TOMAR, G. 2019 Secondary breakup of drops at moderate Weber numbers: effect of density ratio and Reynolds number. *Intl J. Multiphase Flow* **117**, 25–41.
- JALAL, M. & MEHRAVARAN, K. 2012 Fragmentation of falling liquid droplets in bag breakup mode. *Intl J. Multiphase Flow* **47**, 115–132.
- JARRAHBASHI, D. & SIRIGNANO, W.A. 2014 Vorticity dynamics for transient high-pressure liquid injection. *Phys. Fluids* **26**, 101304.
- JEON, S., KIM, S. & PARK, G. 2011 Numerical study of condensing bubble in subcooled boiling flow using volume of fluid model. *Chem. Engng Sci.* **66**, 5899–5909.
- JOHANSEN, H. & COLELLA, P. 1998 A cartesian grid embedded boundary method for Poisson’s equation on irregular domains. *J. Comput. Phys.* **147**, 60–85.
- KHARE, P., MA, D., CHEN, X. & YANG, V. 2013 Phenomenology of secondary breakup of Newtonian liquid droplets. In *50th AIAA Aerospace Sciences Meeting including the New Horizons Forum and Aerospace Exposition*, AIAA Paper 2012-0171.
- LEBAS, R., BEAU, P., BLOKKEEL, G. & DEMOULIN, F. 2006 ELSA model for atomization: to benefit of the eulerian and lagrangian descriptions of the liquid phase. In *Proceedings of the ASME 2006 2nd Joint U.S.–European Fluids Engineering Summer Meeting Collocated With the 14th International Conference on Nuclear Engineering*, vol. 1, Symposia, Parts A and B. Miami, ASME, FL, USA (July 17–20, 2006), pp. 565–572.
- LEE, M.S., RIAZ, A. & AUTE, V. 2017 Direct numerical simulation of incompressible multiphase flow with phase change. *J. Comput. Phys.* **344**, 381–418.
- LIN, S.P. & LIAN, Z.W. 1990 Mechanisms of the breakup of liquid jets. *AIAA J.* **28**, 120–126.
- LINNE, M., PACIARONI, M., HALL, T. & PARKER, T. 2006 Ballistic imaging of the near field in a diesel spray. *Exp. Fluids* **40**, 836–846.
- LIU, X., XUE, R., RUAN, Y., CHEN, L., ZHANG, X. & HOU, Y. 2017 Effects of injection pressure difference on droplet size distribution and spray cone angle in spray cooling of liquid nitrogen. *Cryogenics* **83**, 57–63.
- MAGDELAINE, Q. 2019a Quentin’s sandbox in Basiliak. Available at: http://basilisk.fr/sandbox/qmagdelaine/phase_change/.
- MAGDELAINE, Q. 2019b Hydrodynamics of heterogeneous liquid films. University Sorbonne.
- MALAN, L. 2018 Direct numerical simulation of free-surface and interfacial flow using the VOF method: cavitating bubble clouds and phase change. PhD Thesis, University of Cape Town.
- O’ROURKE, P.J. & AMSDEN, A.A. 1987 The tab method for numerical calculation of spray droplet breakup. *SAE Tech. Paper* 872089.
- PAN, L., TAN, Z., CHEN, D. & XUE, L. 2012 Numerical investigation of vapor bubble condensation characteristics of subcooled flow boiling in vertical rectangular channel. *Nucl. Engng Des.* **248**, 126–136.
- PATTERSON, M.A. & REITZ, R.D. 1998 Modeling the effects of fuel spray characteristics on diesel engine combustion and emission. *SAE Trans.* 27–43.
- POPINET, S. 2003 Gerris: a tree-based adaptive solver for the incompressible Euler equations in complex geometries. *J. Comput. Phys.* **190**, 572–600.
- POPINET, S. 2009 An accurate adaptive solver for surface-tension-driven interfacial flows. *J. Comput. Phys.* **228**, 5838–5866.

Effect of phase change on jet atomization

- REITZ, R. 1987 Modeling atomization processes in high-pressure vaporizing sprays. *Atomiz. Spray Technol.* **3**, 309–337.
- RUEDA VILLEGAS, L., ALIS, R., LEPILLIEZ, M. & TANGUY, S. 2016 A ghost fluid/level set method for boiling flows and liquid evaporation: application to the Leidenfrost effect. *J. Comput. Phys.* **316**, 789–813.
- SALVADOR, F.J., RUIZ, S., CRIALESI-ESPOSITO, M. & BLANQUER, I. 2018 Analysis on the effects of turbulent inflow conditions on spray primary atomization in the near-field by direct numerical simulation. *Intl J. Multiphase Flow* **102**, 49–63.
- SATO, Y. & NIČENO, B. 2013 A sharp-interface phase change model for a mass-conservative interface tracking method. *J. Comput. Phys.* **249**, 127–161.
- SCARDOVELLI, R. & ZALESKI, S. 1999 Direct numerical simulation of free-surface and interfacial flow. *Annu. Rev. Fluid Mech.* **31**, 567–603.
- SCARDOVELLI, R. & ZALESKI, S. 2000 Analytical relations connecting linear interfaces and volume fractions in rectangular grids. *J. Comput. Phys.* **164**, 228–237.
- SCRIVEN, L.E. 1959 On the dynamics of phase growth. *Chem. Engng Sci.* **10**, 1–13.
- SHAO, C., LUO, K. & FAN, J. 2017 Detailed numerical simulation of unsteady drag coefficient of deformable droplet. *Chem. Engng J.* **308**, 619–631.
- SHINJO, J. & UMEMURA, A. 2010 Simulation of liquid jet primary breakup: dynamics of ligament and droplet formation. *Intl J. Multiphase Flow* **36**, 513–532.
- SHINJO, J. & UMEMURA, A. 2011a Surface instability and primary atomization characteristics of straight liquid jet sprays. *Intl J. Multiphase Flow* **37**, 1294–1304.
- SHINJO, J. & UMEMURA, A. 2011b Detailed simulation of primary atomization mechanisms in diesel jet sprays (isolated identification of liquid jet tip effects). *Proc. Combust. Inst.* **33**, 2089–2097.
- TANGUY, S., MÉNARD, T. & BERLEMONT, A. 2007 A level set method for vaporizing two-phase flows. *J. Comput. Phys.* **221**, 837–853.
- TAVANGAR, S., HASHEMABADI, S.H. & SABERIMOGHADAM, A. 2015 CFD simulation for secondary breakup of coal–water slurry drops using OpenFOAM. *Fuel Process. Technol.* **132**, 153–163.
- URNS, S.R. 1996 *An Introduction to Combustion—Concepts and Application*. McGraw-Hill.
- WADHWA, A.R., MAGI, V. & ABRAHAM, J. 2007 Transient deformation and drag of decelerating drops in axisymmetric flows. *Phys. Fluids* **19**, 113301.
- WANG, Z., LI, Y., WANG, C., XU, H. & WYSZYNSKI, M.L. 2016 Experimental study on primary breakup of diesel spray under cold start conditions. *Fuel* **183**, 617–626.
- WANG, Y. & YANG, V. 2019 Vaporization of liquid droplet with large deformation and high mass transfer rate, I: constant-density, constant-property case. *J. Comput. Phys.* **392**, 56–70.
- WELCH, S.W.J. & WILSON, J. 2000 A volume of fluid based method for fluid flows with phase change. *J. Comput. Phys.* **160**, 662–682.
- WEYMOUTH, G.D. & YUE, D.K.P. 2010 Conservative volume-of-fluid method for free-surface simulations on Cartesian-grids. *J. Comput. Phys.* **229**, 2853–2865.
- YANG, H.Q. 1992 Asymmetric instability of a liquid jet. *Phys. Fluids A: Fluid Dyn.* **4**, 681–689.
- YANG, W., JIA, M., SUN, K. & WANG, T. 2016 Influence of density ratio on the secondary atomization of liquid droplets under highly unstable conditions. *Fuel* **174**, 25–35.
- YANG, X. & TURAN, A. 2017 Simulation of liquid jet atomization coupled with forced perturbation. *Phys. Fluids* **29**, 022103.
- ZANDIAN, A., SIRIGNANO, W.A. & HUSSAIN, F. 2017 Planar liquid jet: early deformation and atomization cascades. *Phys. Fluids* **29**, 062109.
- ZANDIAN, A., SIRIGNANO, W.A. & HUSSAIN, F. 2018 Understanding liquid-jet atomization cascades via vortex dynamics. *J. Fluid Mech.* **843**, 293–354.
- ZANDIAN, A., SIRIGNANO, W.A. & HUSSAIN, F. 2019 Vorticity dynamics in a spatially developing liquid jet inside a co-flowing gas. *J. Fluid Mech.* **877**, 429–470.